Article

Cell Stem Cell

Induction of Expansion and Folding in Human Cerebral Organoids

Graphical Abstract

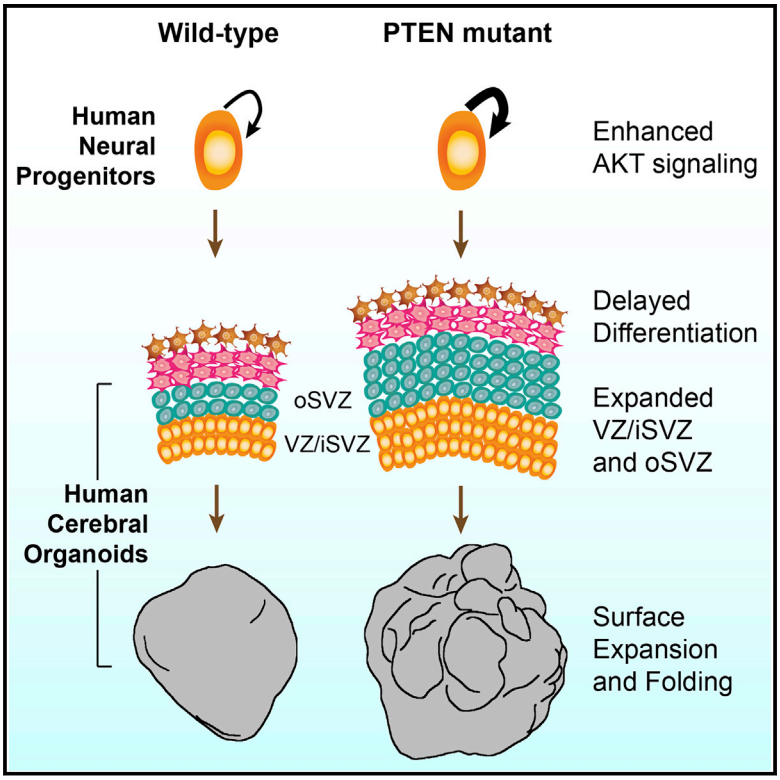

Authors

Yun Li, Julien Muffat, Attya Omer, ..., Lee Gehrke, Juergen A. Knoblich, Rudolf Jaenisch

Correspondence

jaenisch@wi.mit.edu

In Brief

The growth and structural formation of the human cortex can be modeled in vitro using cerebral organoids. In this article, Li, Muffat, and colleagues show that enhancing the PTEN-AKT signaling pathway leads to the generation of human cerebral organoids that are expanded in size and display surface folding.

Highlights

- PTEN deletion enhances human NP proliferation and sensitivity to growth factors
- PTEN mutant human, but not mouse, cerebral organoids display surface folding
- Folded human organoids contain expanded ventricular and outer progenitors
- Zika virus impairs the formation of expanded and folded human cerebral organoids

Li et al., 2017, Cell Stem Cell *20*, 385–396
March 2, 2017
http://dx.doi.org/10.1016/j.stem.2016.11.017

CellPress

Cell Stem Cell
Article

Induction of Expansion and Folding in Human Cerebral Organoids

Yun Li,[1,8] Julien Muffat,[1,8] Attya Omer,[1] Irene Bosch,[2] Madeline A. Lancaster,[3] Mriganka Sur,[4] Lee Gehrke,[2,5,6] Juergen A. Knoblich,[3] and Rudolf Jaenisch[1,7,9,*]
[1]The Whitehead Institute for Biomedical Research, 9 Cambridge Center, Cambridge, MA 02142, USA
[2]Institute for Medical Engineering and Science, Massachusetts Institute of Technology, Cambridge, MA 02139, USA
[3]Institute of Molecular Biotechnology of the Austrian Academy of Sciences, 1030 Vienna, Austria
[4]The Picower Institute for Learning and Memory, Cambridge, MA 02139, USA
[5]Department of Microbiology and Immunobiology, Harvard Medical School, Boston, MA 02115, USA
[6]Harvard-MIT Program in Health Sciences and Technology, Cambridge, MA 02139, USA
[7]Department of Biology, Massachusetts Institute of Technology, 31 Ames Street, Cambridge, MA 02139, USA
[8]Co-first author
[9]Lead Contact
*Correspondence: jaenisch@wi.mit.edu
http://dx.doi.org/10.1016/j.stem.2016.11.017

SUMMARY

An expansion of the cerebral neocortex is thought to be the foundation for the unique intellectual abilities of humans. It has been suggested that an increase in the proliferative potential of neural progenitors (NPs) underlies the expansion of the cortex and its convoluted appearance. Here we show that increasing NP proliferation induces expansion and folding in an in vitro model of human corticogenesis. Deletion of *PTEN* stimulates proliferation and generates significantly larger and substantially folded cerebral organoids. This genetic modification allows sustained cell cycle re-entry, expansion of the progenitor population, and delayed neuronal differentiation, all key features of the developing human cortex. In contrast, *Pten* deletion in mouse organoids does not lead to folding. Finally, we utilized the expanded cerebral organoids to show that infection with Zika virus impairs cortical growth and folding. Our study provides new insights into the mechanisms regulating the structure and organization of the human cortex.

INTRODUCTION

A massive increase in the size of the human cerebral neocortex is accompanied by the expansion of the cortical area, and the associated emergence of extensive cortical folding (Bystron et al., 2008; Geschwind and Rakic, 2013; Sun and Hevner, 2014). In the developing human cerebral cortex, radial glial cells, residing in both the ventricular zone (VZ) and the later-formed sub-ventricular zone (SVZ), give rise to intermediate progenitors and, ultimately, post-mitotic neurons (Lui et al., 2011; Rakic, 1988), following an inside-out pattern of migration (Rakic, 1974). Compared with mice, the developing cortex of humans and other gyrencephalic mammals harbor a larger VZ and SVZ, which are composed of substantially more radial glial cells and intermediate progenitors (Hansen et al., 2010). Whether this increase in neural progenitor (NP) population is directly responsible for the expansion of the human cortex and the evolutionary transformation of a smooth, unfolded cortex to a profoundly folded one remains mostly untested, in no small part because of the inaccessible nature of the developing human cortex. However, recent advances in human pluripotent stem cell technology (Takahashi et al., 2007; Yu et al., 2007) and 3D culture systems (Lancaster et al., 2013; Sasai, 2013) have opened new avenues to investigate human cortical development. Starting with human embryonic stem cells (hESCs) and induced pluripotent stem cells, we have recently reported the generation of cerebral organoids that self-organize into neuralized structures resembling the early developing human cerebral cortex (Lancaster et al., 2013). These in vitro-derived neural tissues recapitulate early stages of cortical formation and display human-specific features such as the outer SVZ. Therefore, human cerebral organoids represent a novel method to investigate the molecular, cellular, and anatomical paradigms of early human cortical development.

Cortical folding can be experimentally induced in the developing mouse brain by β-catenin overexpression (Chenn and Walsh, 2002), inhibition of apoptosis (Kuida et al., 1996, 1998), or modification of NP-specific genes such as *Trnp1* (Stahl et al., 2013) and Arhgap11b (Florio et al., 2015), all likely via direct regulation of the proliferation, survival, and differentiation propensity of NPs. Differential regulation of NP proliferation may also contribute to human-specific cortical pattern formation (Bae et al., 2014). Interestingly, multiple lines of evidence have converged to suggest a physiological involvement of growth factor signaling in regulating human-specific cortical expansion and folding. Introduction of FGF2 into the developing mouse cortex leads to regional formation of gyri (Rash et al., 2013), and human fetal cortical transcriptome revealed progenitor-specific enrichment of platelet-derived growth factor D (*PDGF-D*) (Lui et al., 2014). Existing human genetic evidence strongly suggests that growth factor signaling, in particular through the PTEN-AKT cascade, regulates human cortical formation. Pathological development of a larger brain (megalencephaly) and/or increased gyrification (polymicrogyria) have been linked to

mutations that activate the pathway in genes such as *AKT3*, *PTEN*, *PIK3CA*, and *PIK3R2* (DiLiberti, 1998; Lee et al., 2012; Marchese et al., 2014; Mirzaa et al., 2013; Poduri et al., 2012; Rivière et al., 2012; Terrone et al., 2016). Conversely, mutations that impair growth factor signaling have been linked to symptoms of human microcephaly (Boland et al., 2007; Juanes et al., 2015). Genetically modified mice carrying corresponding mutations were shown to mimic, but frequently to a lesser extent, aspects of the phenotypes displayed by human patients. For example, although *AKT3*-activating mutations have been linked to human macrocephaly and polymicrogyria (Lee et al., 2012; Poduri et al., 2012), *Akt3* mutant mice with increased signaling activity displayed increased brain size but otherwise normal cortical patterning with no increase in gyrification (Tokuda et al., 2011). Similarly, *Pten* mutant mice also displayed macrocephaly without increased gyrification (Groszer et al., 2001; Kwon et al., 2006; Lehtinen et al., 2011). Such phenotypic differences may reflect inherent species differences in signaling regulation, cellular response, and anatomical organization. Therefore, the human genetic evidence strongly suggests an intrinsic and possibly preferential dependence of human NPs on the growth factor signaling cascade.

In the present study, we investigated the direct effect of enhancing human NP proliferation on cortical formation in a 3D cerebral organoid system. We chose the *PTEN* gene because of the human genetics evidence demonstrating its function in cortical development and a substantial body of literature on its role in regulating progenitor cells of various lineages (Hill and Wu, 2009). *PTEN* heterozygous loss-of-function mutations have been associated with human macrocephaly (Butler et al., 2005; Marchese et al., 2014). In the current 3D cerebral organoid system, *PTEN* homozygous mutation was adopted to drive the activation of the phosphoinositide 3-kinase (PI3K)-AKT pathway. Indeed, deletion of the *PTEN* gene increased AKT activity in human NPs, promoted cell cycle re-entry, and transiently delayed neuronal differentiation, resulting in a marked expansion of the radial glia and intermediate progenitor population. Both human and mouse organoids that lacked *PTEN* showed a significant increase in size, but only human organoids displayed substantial surface folding. The degree of expansion and folding was regulated by further tuning the strength of AKT signaling with reduced signaling resulting in smaller and smooth organoids and increased signaling in larger and more folded organoids. These findings lend support to the notion that an increase in the proliferative potential of NPs contributes to the expansion of the human cerebral neocortex and the emergence of surface folding. Last, in light of the current global health emergency regarding Zika virus (ZIKV), we applied the expanded cerebral organoid culture system to investigate a possible link between ZIKV exposure and cortical malformations such as microcephaly and lissencephaly.

RESULTS

PTEN Deletion Enhances Growth Factor-Dependent Proliferation in 2D-Cultured Human Neural Progenitors

To disrupt the human *PTEN* gene, single guide RNA (sgRNA) was designed to target the first exon (Figure 1A), mimicking a recently reported macrocephalic patient mutation (Figure S1A; Marchese et al., 2014). WIBR3, a previously well characterized hESC line (Lengner et al., 2010), was targeted to generate homozygous frameshift mutations using clustered regularly interspaced short palindromic repeats (CRISPR)/Cas9 (Figure 1A). The absence of PTEN protein was confirmed by immunoblotting (Figure 1B). Using the same approach, two additional hESC lines (WIBR1 and WIBR2) were also targeted to generate mutant clones on these independent genetic backgrounds (Figures S1B–S1G).

PTEN and its downstream signaling pathway are involved in the regulation of proliferation, differentiation, and apoptosis of various stem/progenitor populations, but little is known of its function in the developing human brain. Analysis of the BrainSpan Atlas of the Developing Human Brain revealed that *PTEN* expression is low in the VZ/SVZ and high in the cortical plate, where differentiated neurons reside, a pattern inversely correlated with the progenitor markers *PAX6* and *TBR2* (Figures S1H–S1K). Similarly, in vitro-derived human NPs express less *PTEN* compared with neurons, suggesting a possible physiological involvement during normal human neural development (Figure S1L). In a 2D adherent culture system, *PTEN* mutant human NPs displayed a significantly higher growth rate in response to low basic fibroblast growth factor (bFGF) (1–5 ng/ml; Figure 1C) and a higher level of cell cycle re-entry, as revealed by 5-ethynyl-2'-deoxyuridine (EdU) pulse-chase assay and Ki67 co-staining (Figures 1D and 1E). Control and mutant NPs had similar proliferation rates in the presence of high bFGF or in the absence of bFGF (Figure 1E). Enhanced proliferation of mutant NPs was also observed in response to low concentrations of PDGF-DD and IGF2, two growth factors implicated in regulating fetal cortical growth (Lehtinen et al., 2011; Lui et al., 2014; Figures S1N and S1O).

Expansion and Folding of *PTEN* Mutant Human Cerebral Organoids

To investigate the effect of *PTEN* deletion on human neural development in a more complex setting, we adopted the cerebral organoid culture system (Lancaster et al., 2013). Consistent with previous reports, hESCs, when differentiated into 3D neural tissues, grew in volume over time and displayed discrete lineage identity (Figures S2A–S2C). At 4 weeks, the organoids were composed mostly of Nestin+ NPs showing a typical radial glial morphology with processes contacting both the apical and basal surfaces of the neuroepithelium. At 8 weeks, these NPs underwent neuronal differentiation and generated a distinct layer of DCX+ neurons located exclusively away from the ventricle, consistent with the apical-basal axis of neural migration (Figure S2C). At 12 weeks and beyond, Nestin+ NPs had greatly diminished, and the organoids were mainly composed of differentiated neurons and glia (Figures S2D and S2E). In wild-type human organoids, *PTEN* gene expression was lower at earlier stages and increased as the organoids differentiated and matured (Figure S1M).

To compare organoid formation of *PTEN* mutant and isogenic control hESCs, equal numbers of dissociated single cells were seeded to form embryoid bodies (EBs). Both control and mutant WIBR3 hESCs generated EBs with comparable overall morphology after 1 week (Figure S3A). At 4 weeks, although control organoids were relatively spherical and smooth, *PTEN* mutant organoids displayed a markedly increased outgrowth

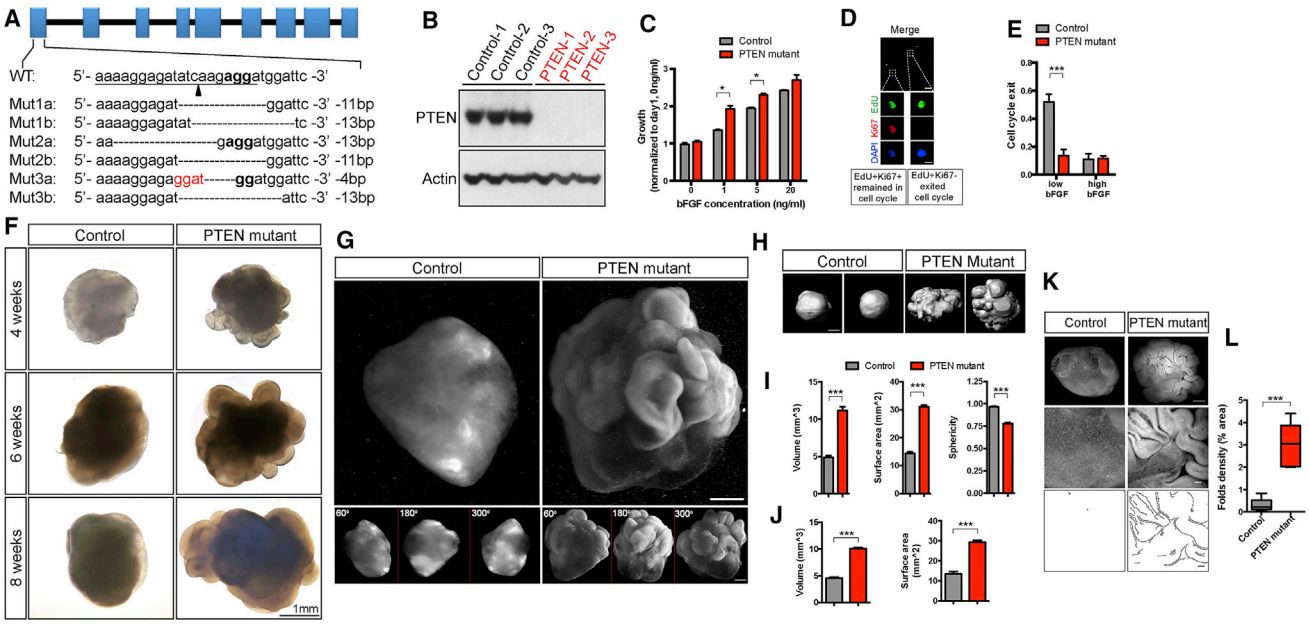

Figure 1. Induction of Expansion and Folding in *PTEN* Mutant Human Cerebral Organoids

(A and B) CRISPR/Cas9-mediated targeting of the human *PTEN* locus, sequences of mutant WIBR3 hESC clones (A), and immunoblotting for PTEN protein (B).

(C) ATP assay on 2D adherent NP culture showing enhanced proliferation in WIBR3 *PTEN* mutants in the presence of low bFGF concentration.

(D and E) Representative image of EdU-Ki67 co-staining in WIBR3 wild-type NPs cultured with low bFGF (D) and quantification of the cell cycle exit ratio (EdU+Ki67−/all EdU+; E). Low bFGF, 1 ng/mL; high bFGF, 10 ng/mL. Scale bars, 50 μm (top) and 10 μm (bottom).

(F and G) Representative bright-field (F) and light sheet images (G) of control and *PTEN* mutant WIBR3 cerebral organoids. Shown at the bottom (G) a different angle view of the main panels above. Scale bars, 1 mm (F) and 500 μm (G).

(H and I) Reconstructed models of control and mutant WIBR3 organoids (H) and quantification of volume, surface area, and sphericity (I). Scale bar, 1 mm.

(J) Quantification of control and mutant WIBR3 organoid volume and surface area on histological sections using the stereological method.

(K and L) Images (K) and quantification (L) of surface fold density in Hoechst-stained control and mutant WIBR3 organoids at 6 weeks. Center (K): higher-magnification view of the top. Bottom (K): algorithmic tracing of surface folds via Canny edge detection. Scale bar, 500 μm (top) and 100 μm (center and bottom).

Results are mean ± SEM. *$p < 0.05$, ***$p < 0.001$. See also Figures S1–S4.

of neuroepithelial tissue surrounding ventricle-like structures (Figure 1F). Neuroepithelial overgrowth was even more evident in mutant organoids at 6 and 8 weeks and led to a drastic increase in size and an overall folded surface (Figure 1F). To better visualize and quantify their 3D morphology, we imaged the organoids on a light sheet fluorescence microscope (Figure 1G). *PTEN* mutants displayed a markedly increased surface area, overall volume, and reduced sphericity compared with controls (Figures 1G–1I). The increases in volume and surface area were separately validated on histological sections (Figure 1J; Figures S3B and S3C). Because the increased surface area was often organized in continuous folds, we further demonstrate a significant increase in fold density in mutant organoids (Figures 1K and 1L). The expansion and folding phenotype was fully penetrant and present in all WIBR3 *PTEN* mutant organoids examined across multiple independent experiments (Figures S3D and S3E) as well as in *PTEN* mutant organoids generated from WIBR1 and WIBR2 hESCs (Figures S4A–S4C).

We explored the potential difference between mouse and human cortical development by generating cerebral organoids from control and *Pten* mutant mouse embryonic stem cells (mESCs). CRISPR/Cas9 gene targeting was used to disrupt the first exon of the *Pten* gene in V6.5 mESCs (Figures S4D and S4E). Three controls and three homozygous frameshift mutants were selected based on genomic sequence and loss of full-length PTEN protein (Figures 2A; Figure S4D). Equal numbers of dissociated single mESCs were used to generate mouse organoids, following an adapted protocol that utilizes similar media and culturing methods as that for human organoids (Eiraku et al., 2008; Lancaster et al., 2013). Compared with controls, *Pten* mutant mouse organoids became progressively larger but remained smooth throughout development with no surface folds (Figures 2B and 2C; Figure S4F). Imaging using a light sheet fluorescence microscope and subsequent quantification demonstrated that *Pten* mutant mouse organoids had increased overall volume but no change in sphericity compared with controls (Figures 2D and 2E). No detectable change in fold density was present in *Pten* mutant mouse organoids (Figure 2F).

PTEN Deletion Expands the Progenitor Pool

We investigated the cellular organizations that underlie the expansion and folding of the *PTEN* mutant human cerebral organoids. At 4 weeks, both control and mutant human organoids were composed of units of continuous neuroepithelium, as revealed by Nestin staining. *PTEN* mutants contained an array of large and sometimes folded neuroepithelial structures (Figure 3A) that expressed NP markers such as Nestin, Pax6, and Sox2 (Figures 3B and 3C). Because the original organoid culture condition

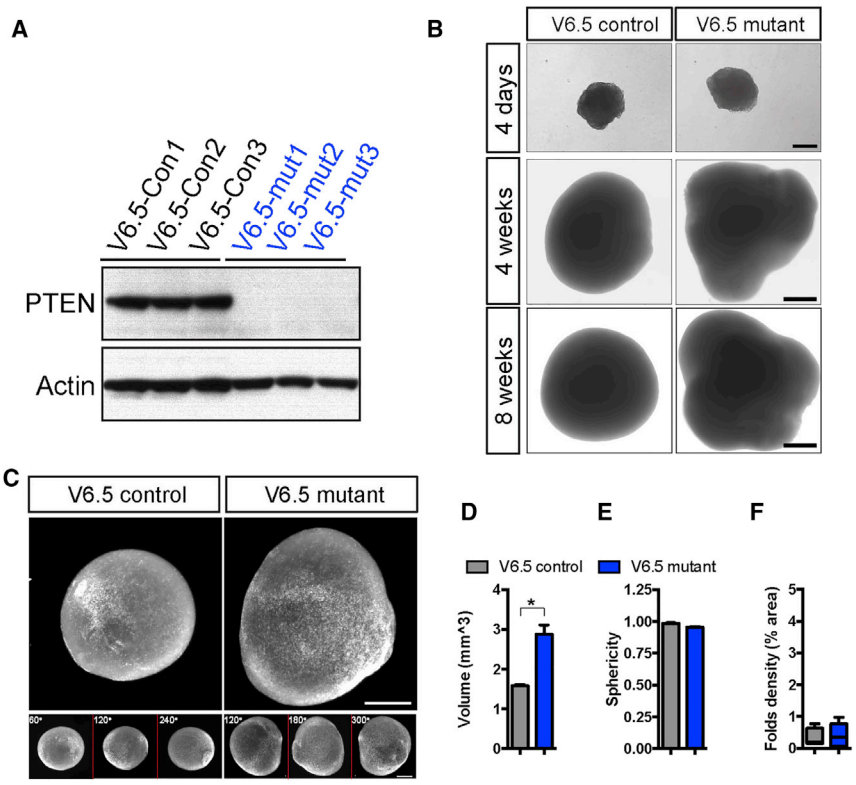

Figure 2. Lack of Folding in *Pten* Mutant Mouse Cerebral Organoids

(A) Immunoblotting shows a complete ablation of wild-type PTEN protein in V6.5 mutant mouse ESCs.

(B and C) Bright-field and light sheet images of control and *Pten* mutant mouse organoids at 4 days, 4 weeks, and 8 weeks. Scale bar, 200 μm (top in B) and 500 μm (middle, bottom in B, and C).

(D–F) Quantification of volume (D), sphericity (E), and fold density (F) on control and *Pten* mutant mouse organoids at 4 weeks.

Results are mean ± SEM. *p < 0.05. See also Figure S4.

provides minimal patterning cues and relies on the intrinsic capacity of hESCs to differentiate into the neural lineage, the majority of the organoids adopt a forebrain identity, as shown by their expression of Pax6 (Figure 3B) and FoxG1 (Figure 7G), but markers of other brain regions can also be observed (Figure S4G). To examine whether organoid expansion and folding can occur from a brain region-specific cellular population, we pre-patterned the EBs specifically toward the dorsal forebrain fate (Li et al., 2013). Treatment with dorsomorphin during the first 7 or 14 days of culture promoted the generation of a dorsal forebrain identity and suppressed markers of other lineages (Figures 3E and 3F; Figures S4H and S4I). At 6 weeks, pre-patterned control forebrain organoids grew to a similar shape and size as un-patterned organoids. Likewise, pre-patterned *PTEN* mutant human forebrain organoids grew larger than controls and developed complex surface folds (Figures 3D and 3G; Figure S4J).

Both control and mutant human organoids contained neuroepithelia organized in a stereotypic manner reminiscent of the early developing cortex, where Ki67+ NPs proliferated at the apical surface of the ventricular zone (Figure 4A). Compared with controls, *PTEN* mutant human organoids harbored significantly more Ki67+ cells at multiple developmental time points (Figures 4A and 4B), further confirmed by qRT-PCR (Figure S5A). Increased proliferation was also observed in *PTEN* mutant organoids derived from WIBR1 and WIBR2 hESCs (Figures S5B–S5D). The enhanced proliferation was prolonged and most prominent at 4–8 weeks and declined over time, with both the control and mutant displaying minimal mitotic activity at 24 weeks (Figure S5A). To investigate the correlation of proliferation and the physical bending of the developing neuroepithelium in *PTEN* mutant human organoids, we measured the distribution of Ki67+ dividing cells relative to their position. We found that areas of the neuroepithelium with an outward curvature contained a significantly higher proportion of proliferating cells compared with un-curved areas (Figures S5E and S5F). This is consistent with the notion that differential proliferation can propel physical buckling and the formation of a curved structure (Kriegstein et al., 2006). Lastly, we found a comparable number and distribution of apoptotic cells within the VZ of control and *PTEN* mutant human organoids (Figures S5G and S5H).

In *PTEN* mutant human organoids, the increase in proliferation coincided with an expansion of the NP pool, as shown by qRT-PCR for radial glia and the intermediate progenitor markers *PAX6*, *ARHGAP11B* (Florio et al., 2015), and *TBR2* (Figures 4C and 4D; Figure S5I) and immunostaining for PAX6, SOX2, and TBR2 (Figures 4F and 4G). Consistent with previous observations, a population of Sox2+ NPs detached from the apical VZ in both control and mutants, coinciding with the presence of the outer radial glia marker HOPX (Figures 4G and 4J). Mutant human organoids harbored significantly more HOPX+ outer radial glial cells; they dispersed into the expanded neuroepithelium in the radial direction (Figures 4G–4I; Figure S5J). Increased abundance of *HOPX* expression in *PTEN* mutant human organoids was further confirmed by qRT-PCR (Figure 4E). A higher proportion of the VZ and outer SVZ progenitors was labeled with Ki67 in mutant organoids (Figures 4J and 4K). Last, *PTEN* mutant human organoids at 12 weeks had increased thickness of the cortical neuroepithelium, further supporting the observation of a radial expansion (Figure 4L). These findings demonstrate that *PTEN* ablation led to expansion of the human NP pool in both the VZ and SVZ.

In contrast to *PTEN* mutant human organoids, *Pten* mutant mouse organoids, which were morphologically smooth, displayed a transient elevation of proliferation over controls, but only within a narrow developmental window (Figures 4M and 4N; Figure S5K). This restricted proliferative capacity of mouse NPs coincides with the smaller steady-state sizes of the mouse organoids compared with human organoids (Figures 1I and 2D). HOPX immunopositivity was absent in mouse

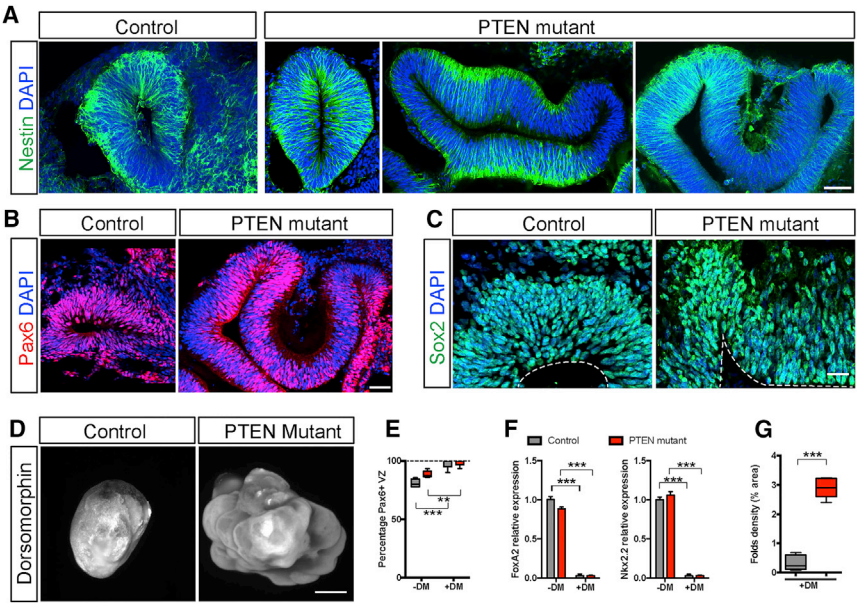

Figure 3. *PTEN* Deletion Induces Expansion and Folding of Forebrain Neuroepithelia in Human Cerebral Organoids

(A–C) Immunostaining for NPs using antibodies against Nestin (A), Pax6 (B), and Sox2 (C) in control and mutant WIBR3 organoids at 4 weeks. Scale bars, 50 μm (A and B) and 20 μm (C).

(D–G) Light sheet images and quantification of control and mutant WIBR3 organoids treated with dorsomorphin (DM) for 14 days, demonstrating expansion and folding (D), increased fold density (G), patterning toward the forebrain fate (E) at the preclusion of non-forebrain lineages (F).

Results are mean ± SEM. $^{**}p < 0.01$, $^{***}p < 0.001$. See also Figure S4.

organoids (Figure 4O). Together, these findings highlight intrinsic disparities between mouse and human NPs in proliferation potential and cellular composition.

PTEN Deletion Elicits a Transient Delay in Neuronal Differentiation

A hallmark difference between primate and rodent cortical development is the duration of proliferation, with primate NPs undergoing many more rounds of cell division prior to committing to terminal differentiation (Kornack and Rakic, 1998). We investigated whether the increased proliferation in *PTEN* mutant human organoids was coupled with changes in differentiation propensity. At 4 weeks, neuronal differentiation was initiated in control organoids, and DCX+ neurons began to emerge (Figure 5A). In contrast, mutant organoids contained predominantly Nestin+ NPs with few neurons (Figure 5A). qRT-PCR and immunoblotting confirmed that mutant organoids had significantly reduced DCX RNA and protein (Figures S6A–S6C). An EdU pulse-chase experiment on 4-week-old organoids showed that mutants had significantly less cell cycle exit after 24 hr (Figures 5B and 5C). A majority of EdU+ cells in mutant organoids were Sox2+ NPs, in contrast to controls, where a substantial fraction had become DCX+ (Figures 5D–5F). A similar finding of delayed neuronal differentiation was seen in *PTEN* mutant human organoids on the WIBR1 and WIBR2 background (Figure S6D). In contrast, DCX+ or Ctip2+ neurons were already abundantly present in 3-week-old mouse control and *Pten* mutant organoids (Figure 4O; Figure S6E).

This delay in neuronal differentiation in *PTEN* mutant human organoids was transient and gradually normalized. At 8 weeks, abundant DCX+ neurons were present, and the majority of cells labeled with EdU at 4 weeks had assumed a neuronal phenotype in both controls and mutants (Figures 5G and 5H; Figures S6F and S6H). A small population of EdU+ cells co-expressed HOPX and resided in the outer SVZ, suggesting their identity as outer radial glia (Figures S6G and S6I). Transcriptional analysis of a panel of genes enriched in NPs and neurons demonstrated reduced expression of neuronal markers in mutants at 4 weeks but normalized expression over time at 10 and 16 weeks (Figures 5I–5K). At 12 weeks, both control and mutant human organoids harbored outer radial glia cells, early- and late-born neurons that were organized in a rudimentary inside-out pattern (Figures 5L–5N). In mature control and mutant human organoids, differentiated neuronal cell types were predominant, and the level of proliferation was diminished (Figure 5K; Figure S5A). At these ages, *PTEN* mutant organoids sustained a folded morphology, underlined by the presence of folded cortical plates composed of differentiated neurons and glia (Figure 5O). We conclude that a transient delay in differentiation allowed amplification of the NP pool and contributed to the expansion and folding of the *PTEN* mutant human organoids.

AKT Activation Mediates the Expansion and Folding of *PTEN* Mutant Human Cerebral Organoids

To confirm that *PTEN* deficiency was responsible for the phenotypes, we transduced mutant hESCs with a lentivirus vector encoding GFP or a PTEN-GFP fusion protein (Figures 6A and 6B) and generated organoids. At 6 weeks, although *GFP*-transduced mutant human organoids were expanded and folded, *PTEN-GFP*-transduced mutants formed smooth organoids (Figure 6C; Figure S7A) and showed normalized levels of proliferation and neuronal differentiation (Figures S7B–S7D).

AKT activation is a well-documented downstream effect of *PTEN* deletion (Worby and Dixon, 2014). *PTEN*, *AKT1*, *AKT2*, and *AKT3* are expressed in the developing human cortex (Figures S1H and S7E). In control human organoids, phospho-AKT (pAKT) could be detected, albeit at a relatively low level (Figures S7F and S7H). *PTEN* deletion led to a significant upregulation of pAKT (Figure 6D; Figures S7F–S7I). In both control and mutants, pAKT-positive staining was enriched in the VZ and co-localized with progenitor markers such as Nestin, Sox2, and phospho-Vimentin (Figure 6D; Figures S7F and S7G). In mature human organoids comprised of mostly differentiated neurons, the pAKT level was reduced but could still be detected with tyramide signal-amplified immunostaining as well as immunoblotting (Figures S7J and S7L). In 12-week-old organoids, acute exposure to exogenous BDNF elicited a rapid

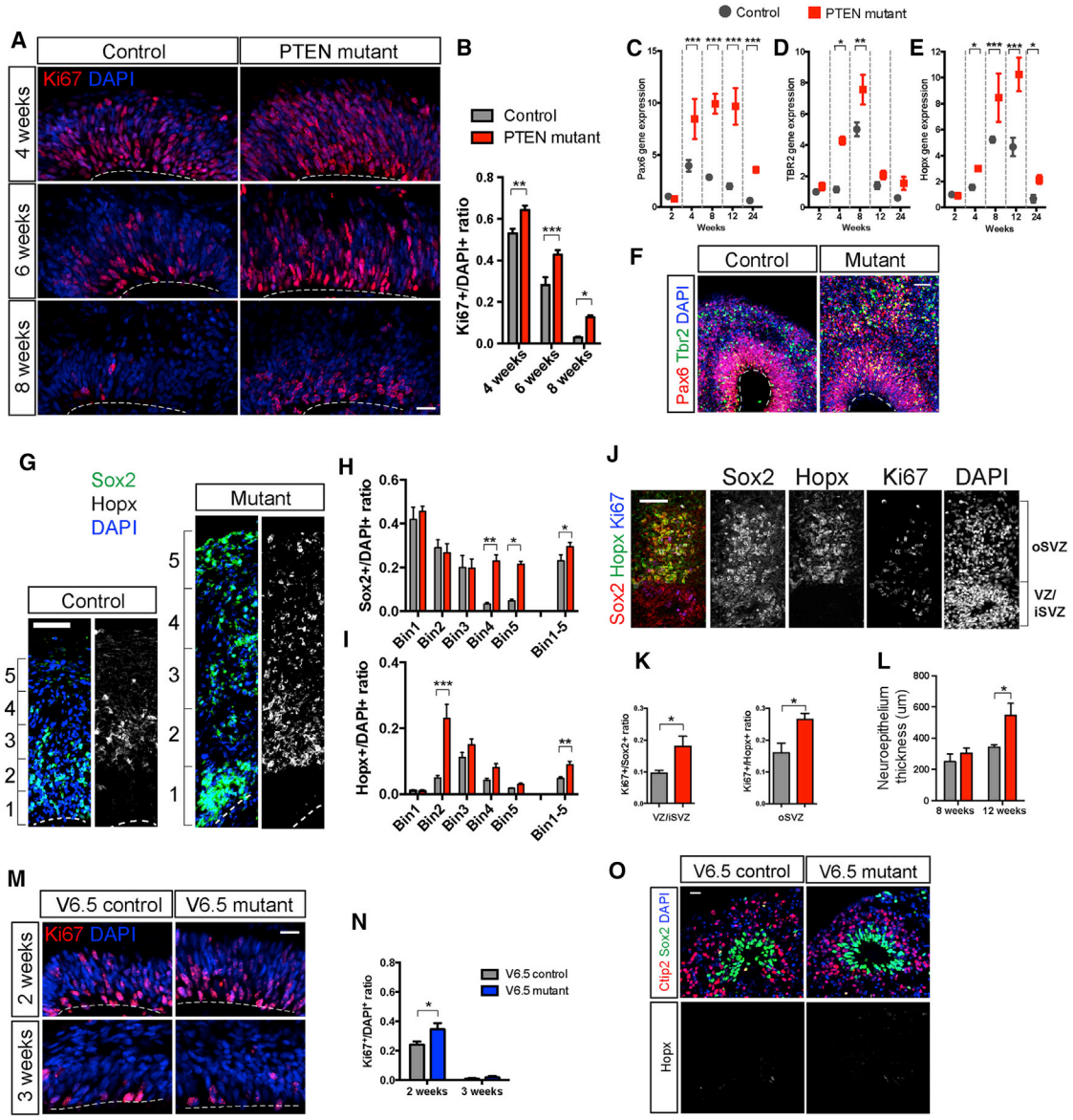

Figure 4. *PTEN* Deletion Enhances Proliferation and Expands the NP Pool

(A and B) Representative images (A) and quantification (B) of Ki67 immunostaining in control and *PTEN* mutant WIBR3 cerebral organoids. Scale bar, 20 μm.

(C–E) Quantitative RT-PCR analysis of the radial glial marker Pax6 (C), the intermediate progenitor marker Tbr2 (D), and the outer radial glia marker Hopx (E) demonstrates their temporally specific overexpression in *PTEN* mutant WIBR3 organoids compared with controls.

(F) Immunostaining for Pax6 and Tbr2 shows increased numbers of positive cells in *PTEN* mutant WIBR3 organoids.

(G–I) Representative images of the expanded neuroepithelium in 12-week-old control and *PTEN* mutant WIBR3 organoids stained with Sox2 and the outer radial glia marker Hopx. Quantification was conducted by measuring and dividing the entire span of the neuroepithelium into five equal portions (bins), showing significantly more Sox2+ (H) and Hopx+ cells (I) in *PTEN* mutant WIBR3 organoids in the expanded neuroepithelium. Scale bar, 100 μm.

(J and K) Representative images of Sox2, Hopx, and Ki67 co-staining in a *PTEN* mutant WIBR3 organoid (J) and quantification showing increased proliferation of VZ/iSVZ (inner sub-ventricular zone) as well as oSVZ (outer sub-ventricular zone) NPs in *PTEN* mutants compared with controls (K).

(L) Total neuroepithelial thickness at 8 and 12 weeks in control and *PTEN* mutant WIBR3 organoids.

(M and N) Representative images (M) and quantification (N) of Ki67 immunostaining in control and *Pten* mutant mouse cerebral organoids. Scale bar, 20 μm.

(O) Immunostaining for the NP marker Sox2, the outer radial glia marker Hopx, and the neuronal marker Ctip2 in 3-week-old control and *Pten* mutant mouse organoids, showing lack of Hopx immunopositivity. Scale bar, 20 μm.

Results are mean ± SEM. *p < 0.05, **p < 0.01, ***p < 0.001. See also Figure S5.

elevation in AKT signaling, suggesting that scarcity of relevant neurotrophic factors in the culture medium may contribute to the reduced baseline pAKT activity (Figures S7K and S7L). This transient and cell type-specific activation of AKT signaling in NPs echoed the pattern of enhanced proliferation in *PTEN* mutant human organoids and strongly indicated that increased

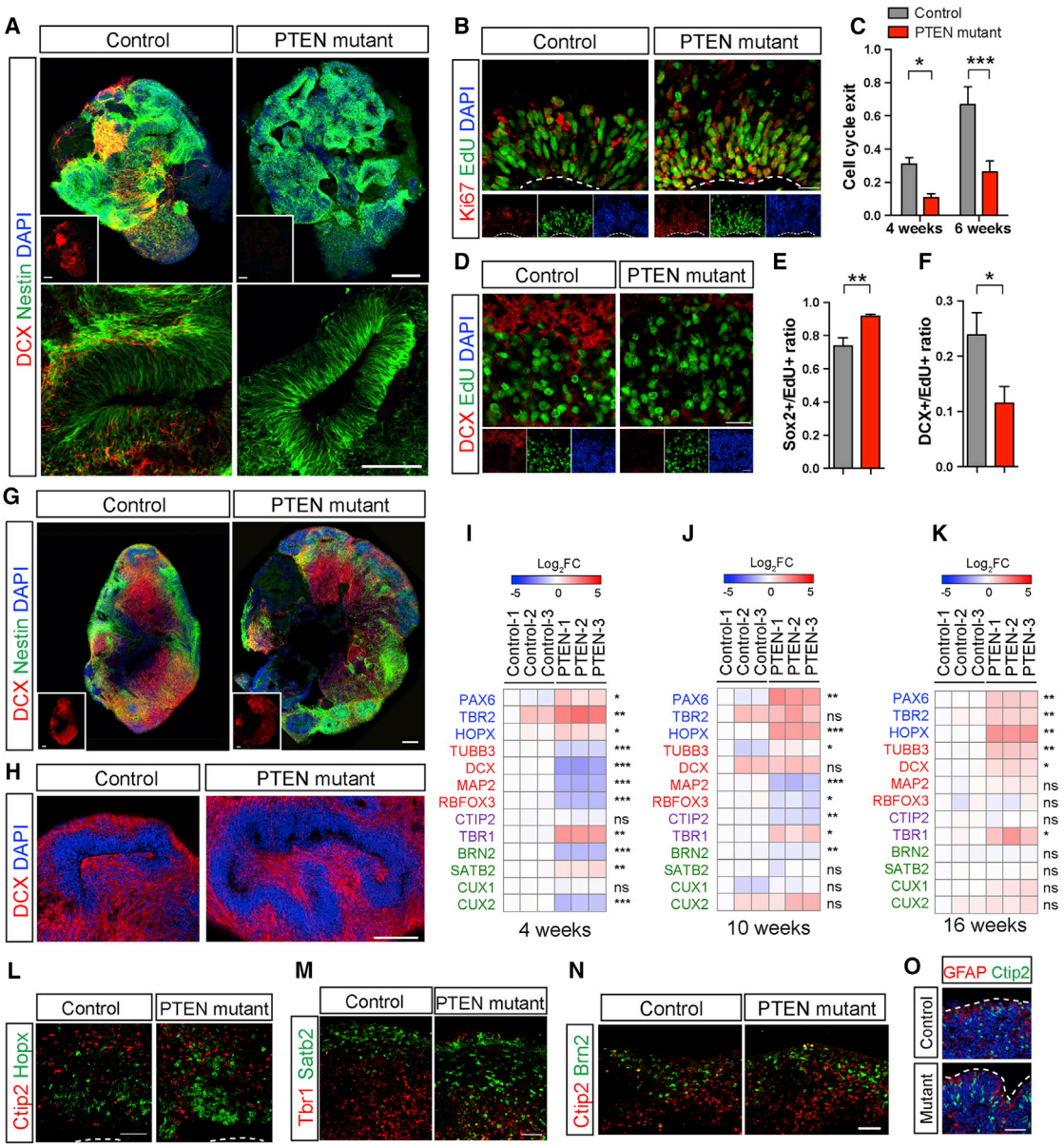

Figure 5. Transient Delay in Neuronal Differentiation Expands the NP Pool

(A) Immunostaining for DCX and Nestin at 4 weeks in control and *PTEN* mutant WIBR3 cerebral organoids. Scale bar, 200 μm.

(B and C) Representative images of EdU-Ki67 co-staining in 4-week-old control and mutant WIBR3 organoids (B) and quantification of the cell cycle exit ratio (EdU+Ki67-/all EdU+) (C) in 4- and 6-week-old organoids. Scale bars, 20 μm.

(D) Immunostaining for DCX and EdU in 4-week-old control and mutant WIBR3 organoids. Scale bars, 20 μm.

(E and F) Quantitative cell fate analysis of EdU+ cells in 4-week-old organoids, showing that *PTEN* mutant EdU+ cells have increased retention as Sox2+ NPs (E) and a decreased propensity for differentiation into DCX+ immature neurons (F).

(G and H) Immunostaining for DCX (G and H) and Nestin (G) at 8 weeks. Scale bar, 200 μm.

(I–K) Differential gene expression analyses by qRT-PCR on control and mutant WIBR3 organoids at 4 (I), 10 (J), and 16 (K) weeks. Genes analyzed are representative of NPs (*PAX6*, *TBR2*, and *HOPX*), pan-neuronal markers (*TUBB3*, *DCX*, *MAP2*, and *RBFOX3*), early-born neurons (*CTIP2* and *TBR1*), and late-born neurons (*BRN2*, *SATB2*, *CUX1*, and *CUX2*). The majority of neuronal markers were transiently downregulated in *PTEN* mutants at 4 weeks but greatly normalized at 16 weeks. Gene expressions are normalized to control-1 at each time point. The p value reflects controls versus mutants.

(L–N) Immunostaining for markers of outer radial glia (Hopx, L), early-born neurons (Tbr1 [M] and Ctip2 [N]), and late-born neurons (Satb2 [M] and Brn2 [N]) in control and mutant WIBR3 organoids at 12 weeks. Scale bars, 50 μm.

(O) *PTEN* mutant WIBR3 organoids had a folded cortical plate at 16 weeks. The images show immunostaining for markers of neurons (Ctip2) and astrocytes (GFAP). White dashed lines outline the cortical surface. Scale bars, 50 μm.

Results are mean ± SEM. *p < 0.05, **p < 0.01, ***p < 0.001. See also Figure S6.

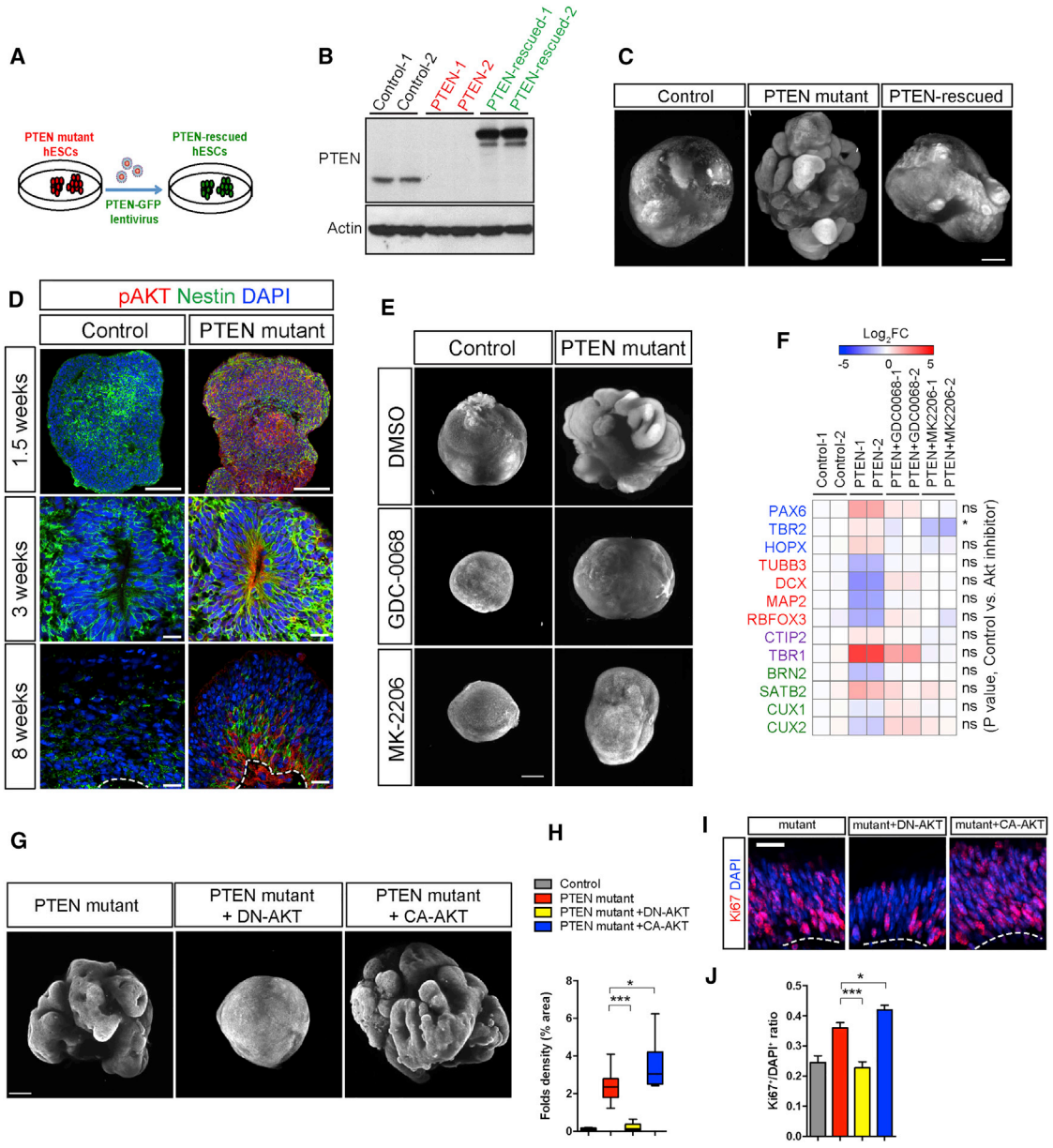

Figure 6. PTEN-AKT Signaling Controls Expansion and Folding in Human Cerebral Organoids

(A) Schematic depicting the strategy to rescue *PTEN* mutant WIBR3 hESCs via lentivirus re-expression of *PTEN*.

(B) Immunoblotting for PTEN shows the presence of PTEN-GFP fusion protein in rescued *PTEN* mutant WIBR3 hESCs.

(C) Light sheet images of Hoechst-stained WIBR3 organoids at 6 weeks, generated from control, *PTEN* mutant, and *PTEN*-rescued hESCs. Scale bar, 500 μm.

(D) Immunostaining images of pAKT and Nestin in control and mutant WIBR3 organoids. Increased pAKT immunostaining is present in mutants at 1.5 weeks, prior to the onset of expansion and folding (top). Increased pAKT signal concentrates in Nestin+ NPs and is highest at the apical surface. Scale bars, 100 μm (top) and 20 μm (center and bottom).

(E) Light sheet images of control and mutant WIBR3 organoids at 6 weeks, treated with AKT inhibitors GDC-0068 (1uM) or MK-2206 (100nM). Scale bar, 500um.

(F) Differential gene expression analyses by quantitative RT-PCR on control and mutant WIBR3 organoids, treated with AKT inhibitors GDC-0068 (1uM) or MK-2206 (100nM). Gene expressions are normalized to control-1. P value reflects controls versus AKT inhibitor treated mutants.

(G) Light sheet images of 6-week-old human organoids generated from *PTEN* mutant WIBR3 alone or transduced with a lentivirus encoding dominant negative (*DN*)-*AKT* or constitutive active (*CA*)-*AKT*. Scale bars, 500um.

(H) Quantitative analysis of the density of surface folds in 6-week-old organoids from *PTEN* mutant alone, or *PTEN* mutant transduced with *DN-AKT* or *CA-AKT*.

(I and J) Representative images (I) and quantification (J) of Ki67 immunostaining in 6-week-old organoids from *PTEN* mutant alone or *PTEN* mutant transduced with *DN-AKT* or *CA-AKT*. Scale bar, 20 μm.

Results are mean ± SEM. *p < 0.05, ***p < 0.001. See also Figure S7.

AKT signaling drove the expansion of the NP pool and, consequently, the expansion and folding of cortical tissue.

To directly investigate whether AKT activation was responsible for the expansion and folding phenotypes, we treated developing *PTEN* mutant human organoids with GDC-0068 or MK-2206, known inhibitors of AKT activation. Although both inhibitors at higher concentrations were deleterious for cellular growth and prevented the formation of viable EBs, lower concentrations allowed the generation of mutant human organoids with comparable size and morphology as non-treated controls (Figure 6E) but blocked the formation of expanded and folded organoids, accompanied by normalized proliferation and neural marker gene expression (Figures 6E and 6F; Figure S7M). Furthermore, a lentivirus-transduced dominant negative form of *AKT* normalized proliferation and blocked the formation of folded neuroepithelium in mutant organoids (Figures 6G–6J). In contrast, a constitutive active form of *AKT* further enhanced proliferation as well as the expansion of neuroepithelium to form organoids with even greater size and surface complexity than the *PTEN* mutant alone (Figures 6G–6J). These findings demonstrate that AKT signaling exerts an essential, tunable control on the expansion and folding of cortical neuroepithelium.

ZIKV Infection Impairs Expansion and Folding in *PTEN* Mutant Cerebral Organoids

The generation of cerebral organoids with more complex, human-like structures enhances our ability to model brain malformation because of genetic or environmental causes. To that end, we applied our 3D culture system to study the consequence of ZIKV infection. Although the underlying mechanism remains to be elucidated, the recent outbreak of ZIKV in Central and South America is associated with severe teratogenic consequences. Accumulating evidence indicates that affected fetuses and newborns display a plethora of neurological abnormalities, including microcephaly, lissencephaly, pachygyria, and cortical atrophy (Hazin et al., 2016). Although recent studies in 2D and 3D human neural cultures have demonstrated the tropism of ZIKV toward NPs and its effect on organoid formation (Cugola et al., 2016; Garcez et al., 2016; Onorati et al., 2016; Qian et al., 2016; Tang et al., 2016), none utilized a 3D culture system that mimics key developmental features of the human cortex, such as expansion and surface folding.

ZIKV exposure during early pregnancy is correlated with risks of major brain malformation, such as microcephaly and lissencephaly. In organoids, ZIKV infection at the onset of surface folding (day 19) leads to widespread initiation of apoptosis (Figures 7A and 7B). 10 days post infection, ZIKV severely hampered organoid growth both in size and surface folding (Figures 7C–7E). Cellular analysis revealed broad detection of viral envelope protein in infected organoids, coinciding with marker of apoptosis (Figure 7C). In contrast, infection with an equal amount of Dengue virus did not trigger increased apoptosis or broad viral amplification (Figures 7B and 7C). Therefore, ZIKV exposure at this early stage severely disrupted organoid expansion and fold formation. We next examined the effect of ZIKV on 4-week-old organoids, when neuronal differentiation is initiated in control organoids and delayed in mutants (Figure 5A). Although a low amount of ZIKV led to partial infection of control organoids at this stage, *PTEN* mutant organoids displayed a markedly increased susceptibility to infection (Figures 7F and 7G). Regions of organoid expansion and folding were amply infected with ZIKV (Figure 7G) and correlated with increased apoptosis (Figure 7H) and decreased proliferation (Figure 7I). Staining for activated caspase on whole mutant organoids further demonstrated a global increase in apoptosis 4 days after ZIKV exposure (Figure 7J). Together, these findings demonstrate the profound consequences of ZIKV exposure during early neural development on the expansion and folding of the developing cortex in vitro and illustrate the strength of the genetically modified cerebral organoid system in modeling complex structural malformations of the developing human brain.

DISCUSSION

Efforts in the investigation of human brain development have been hindered by a lack of access to the fetal human brain. Given the substantial species difference between humans and the currently available model organisms pertinent to cortical morphology and function, it is essential to develop an alternative in vitro system that recapitulates key features of human cortical formation. Here, using a genetically modified cerebral organoid system, we address the direct consequences of increased proliferation in human cortical development. Compared with control organoids, *PTEN* mutant human organoids develop a markedly expanded VZ/SVZ, increased overall size, and a larger surface area organized into continuous cortical folds. This in vitro expansion is triggered by increased proliferation, transiently delayed neuronal differentiation, and, thereby, an amplified overall NP population. Such amplification abides by the cellular and anatomical identity of the human developing cortex and results in a greater number of NPs first in the VZ and, subsequently, in the outer SVZ. In *PTEN* mutant human organoids, the genetically modified neural tissue expands tangentially to generate longer sheets of neuroepithelium and radially to form thicker neuroepithelium. Such modes of in vitro structural expansion are consistent with the radial unit hypothesis of neocortical expansion (Rakic, 1988), suggesting that increased proliferation contributes to folding. We envision future work to incorporate spatially and temporally specific control of the PTEN-AKT signaling pathway to drive NP proliferation in an inducible and reversible manner, allowing the precise dissection of the contribution of tangential and radial expansion to cortical expansion and folding.

The comparison of mouse and human organoids revealed a marked species difference in the capacity of developing expanded and folded neural tissues. In contrast to the drastic effects of *PTEN* deletion in human organoids, *Pten* mutant mouse organoids grew larger but did not form surface folds, coinciding with a short window of enhanced proliferation and a lack of an outer SVZ. The smooth appearance of mouse *Pten* mutant organoids echoes the lack of cortical folding in *Pten* mutant mouse brains, further indicating that features inherent to human NPs, such as the capacity of a prolonged period of proliferation and the generation of an outer radial glia population, may underlie human-specific cortical tissue expansion and folding. Recent studies in mice demonstrated that overexpression of *ARHGAP11B*, a human-specific gene enriched in the NPs of the developing cortex, can endow mouse NPs with enhanced proliferation, leading to the emergence of cortical folding (Florio

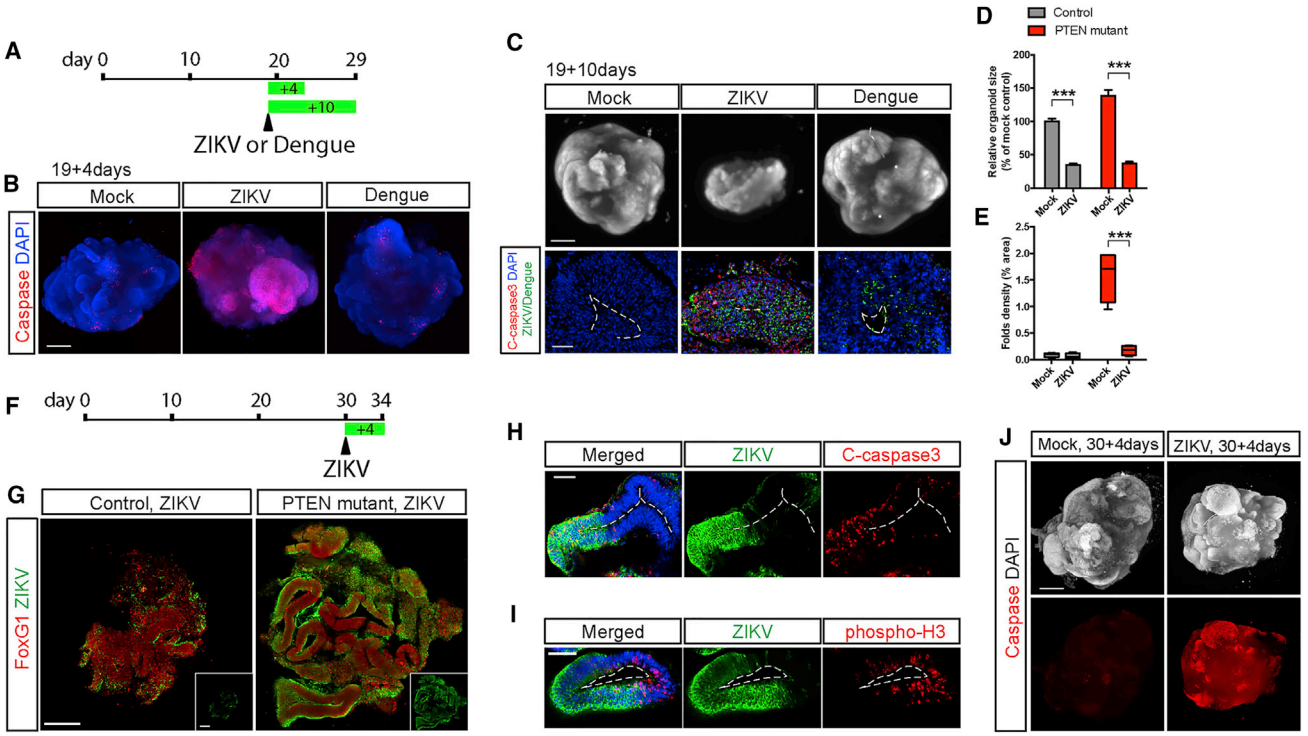

Figure 7. ZIKV Infection Impairs Expansion and Folding in Human Cerebral Organoids

(A and B) Schematic (A) and light sheet images (B) of *PTEN* mutant WIBR3 cerebral organoids on day 23 (19 + 4 days) showing widespread caspase activity induced by ZIKV but not Dengue virus. Scale bar, 500 μm.

(C) Light sheet images and immunostaining of mutant WIBR3 organoids on day 29 (19 + 10 days) show reduced organoid size and increased apoptosis caused by ZIKV but not Dengue virus. C-caspase 3, cleaved caspase 3 as detected by immunostaining. Scale bars, 500 μm (top) and 50 μm (bottom).

(D and E) Quantitative analysis of organoids on day 29 (19 + 10 days) shows reduced size (D) and loss of surface fold density (E) upon ZIKV exposure.

(F and G) Schematic (F) and representative images (G) of immunostaining for ZIKV-infected control and mutant WIBR3 organoids on day 34 (30 + 4 days). Scale bar, 200 μm.

(H and I) Representative images of immunostaining in mutant WIBR3 organoids show that ZIKV infection coincides with elevated apoptosis (cleaved caspase 3, H) and reduced proliferation (phosphorylated H3, I). Scale bars, 50 μm.

(J) Light sheet images show that mutant WIBR3 organoids treated with ZIKV on day 30 displayed widespread apoptosis, as revealed by whole-mount caspase activity staining. Scale bar, 500 μm.

Results are mean ± SEM. ***$p < 0.001$.

et al., 2015). These findings raise the possibility that further genetic engineering may shed light on the mechanism and plasticity of mouse and human cortical development.

Our study highlights the essential role for the PTEN-AKT signaling pathway in regulating human neural development. Gain- and loss-of-function mutations of genes in this pathway have been reported in patients with major brain malformation (Boland et al., 2007; DiLiberti, 1998; Juanes et al., 2015; Lee et al., 2012; Marchese et al., 2014; Mirzaa et al., 2013; Poduri et al., 2012; Rivière et al., 2012; Terrone et al., 2016), suggesting that a precise level of AKT activity is pivotal to brain formation. Our study in human organoids demonstrates that AKT activity is enriched in the NP population in both control and mutants. Inhibition of AKT activity via pharmacological or genetic means results in smaller organoids, reminiscent of microcephaly in patients with *AKT* heterozygous loss-of-function mutation (Boland et al., 2007). We note that, unlike NPs, *PTEN* mutant mature neurons within the organoids display less AKT activity. Acute stimulation with BDNF was sufficient to increase AKT activity, suggesting the reduced basal AKT activity may stem from the lack of neurotrophic growth factors in the current culture system. Future investigation of the effects of AKT activation in response to various trophic factors in mature human neurons could provide novel insights into normal and pathological neural functions. Another limitation of the current culture system is that it inadequately reflects human fetal brain development because it does not support the formation of folded non-mutant human cerebral organoids. This is not surprising, considering its historical origin from the minimal culture media aimed at supporting the survival and differentiation of mouse NPs and EBs (Eiraku et al., 2008). We found that activating the PTEN-AKT pathway, a central signaling cascade downstream of various growth factors, is sufficient to induce folding. Interestingly, embedding in an extracellular matrix (Matrigel) rich in growth factors spurs a rapid yet transient phase of growth in both wild-type and mutant human organoids. Thus, it is likely that a combination of physiologically relevant growth factors could also induce folding in wild-type human organoids. Further microfluidic and microfabrication designs can be implemented to improve oxygen and nutrient exchange, maintain tissue health and homeostasis,

and provide more faithful recapitulation of the in vivo developmental process.

In the current study, we utilized an isogenic genetic system to demonstrate that the cerebral organoid system allows experimental manipulation of distinct, isolated driving forces of cortical development such as proliferation. This experimental framework can be broadly utilized to model other genetic and environmental factors that determine the size and shape of a developing human cortex and explore pathological cortical formation such as microcephaly, macrocephaly, polymicrogyria, lissencephaly, and double cortex syndrome. We used this system to model microcephaly and lissencephaly resulting from ZIKV exposure. Our findings revealed major organoid growth and folding defects because of ZIKV but not Dengue virus exposure, indicating a strong pathological difference between these two closely related flaviviruses.

STAR★METHODS

Detailed methods are provided in the online version of this paper and include the following:

- KEY RESOURCES TABLE
- CONTACT FOR REAGENT AND RESOURCE SHARING
- EXPERIMENTAL MODEL AND SUBJECT DETAILS
  - ESC culture
- METHOD DETAILS
  - Neural differentiation
  - CRISPR/Cas9 gRNA design
  - CRISPR/Cas9-mediated genome editing of ESCs
  - Cerebral organoid culture
  - Lentivirus production and transduction
  - ZIKV and Dengue virus production and infection
  - ATP assay
  - EdU click-it assay
  - Histology and imaging
  - RNA extraction, reverse transcription and quantitative PCR
  - Protein purification and immuno-blotting
  - Analysis of BrainSpan data
- QUANTIFICATION AND STATISTICAL ANALYSIS

SUPPLEMENTAL INFORMATION

Supplemental Information includes seven figures and two tables and can be found with this article online at http://dx.doi.org/10.1016/j.stem.2016.11.017.

AUTHOR CONTRIBUTIONS

Y.L., J.M., and R.J. conceived the project, designed the experiments, interpreted the results, and wrote the paper with input from all authors. A.O. participated in cell culture, sample preparation, and data analysis. I.B. and L.G. provided Zika and Dengue viruses for the study and participated in the design of the virus infection experiments. M.A.L., J.A.K., and M.S. advised on the study design and helped establish the organoid culture system.

ACKNOWLEDGMENTS

The authors thank Dongdong Fu, Raaji Alagappan, Tenzin Lungjangwa, Sean Corcoran, Laure Freland, and Grisilda Bakiasi for technical support and Danielle Feldman and members of the Jaenisch lab for helpful discussions. We thank Magdalena Renner for advice on cerebral organoid cultures; Wendy Salmon, Dr. Christian Cortes Campos, and Dr. Ryann Fame for help with light sheet imaging; Dr. Bryan Luikart for the *PTEN-GFP* plasmid; and Dr. Michael Robinson for the *AKT* plasmids. Y.L. received funding from a Simons Foundation postdoctoral fellowship, an International Rett Syndrome Foundation postdoctoral fellowship, and a NARSAD Young Investigator Grant from the Brain and Behavior Research Foundation. J.M. received support from the European Leukodystrophy Association and a NARSAD Young Investigator Grant from the Brain and Behavior Research Foundation. A.O. was supported by a Jerome and Florence Brill Graduate Student Fellowship. Work in the R.J. laboratory was supported by grants from the Simons Foundation (SFARI 204106 and SFLIFE 286977); NIH Grants HD 045022, R01-MH104610, and R01-NS088538; the ELA Foundation; the Emerald Foundation; Biogen; and the Simons Center for the Social Brain at MIT. Work in the L.G. laboratory was supported by NIH AI100190. R.J. is an advisor to Stemgent and a cofounder of Fate Therapeutics and Fulcrum Therapeutics.

Received: September 6, 2016
Revised: October 24, 2016
Accepted: November 29, 2016
Published: December 29, 2016

REFERENCES

Bae, B.I., Tietjen, I., Atabay, K.D., Evrony, G.D., Johnson, M.B., Asare, E., Wang, P.P., Murayama, A.Y., Im, K., Lisgo, S.N., et al. (2014). Evolutionarily dynamic alternative splicing of GPR56 regulates regional cerebral cortical patterning. Science *343*, 764–768.

Boland, E., Clayton-Smith, J., Woo, V.G., McKee, S., Manson, F.D., Medne, L., Zackai, E., Swanson, E.A., Fitzpatrick, D., Millen, K.J., et al. (2007). Mapping of deletion and translocation breakpoints in 1q44 implicates the serine/threonine kinase AKT3 in postnatal microcephaly and agenesis of the corpus callosum. Am. J. Hum. Genet. *81*, 292–303.

Butler, M.G., Dasouki, M.J., Zhou, X.P., Talebizadeh, Z., Brown, M., Takahashi, T.N., Miles, J.H., Wang, C.H., Stratton, R., Pilarski, R., and Eng, C. (2005). Subset of individuals with autism spectrum disorders and extreme macrocephaly associated with germline PTEN tumour suppressor gene mutations. J. Med. Genet. *42*, 318–321.

Bystron, I., Blakemore, C., and Rakic, P. (2008). Development of the human cerebral cortex: Boulder Committee revisited. Nat. Rev. Neurosci. *9*, 110–122.

Chenn, A., and Walsh, C.A. (2002). Regulation of cerebral cortical size by control of cell cycle exit in neural precursors. Science *297*, 365–369.

Cugola, F.R., Fernandes, I.R., Russo, F.B., Freitas, B.C., Dias, J.L., Guimarães, K.P., Benazzato, C., Almeida, N., Pignatari, G.C., Romero, S., et al. (2016). The Brazilian Zika virus strain causes birth defects in experimental models. Nature *534*, 267–271.

DiLiberti, J.H. (1998). Inherited macrocephaly-hamartoma syndromes. Am. J. Med. Genet. *79*, 284–290.

Eiraku, M., Watanabe, K., Matsuo-Takasaki, M., Kawada, M., Yonemura, S., Matsumura, M., Wataya, T., Nishiyama, A., Muguruma, K., and Sasai, Y. (2008). Self-organized formation of polarized cortical tissues from ESCs and its active manipulation by extrinsic signals. Cell Stem Cell *3*, 519–532.

Florio, M., Albert, M., Taverna, E., Namba, T., Brandl, H., Lewitus, E., Haffner, C., Sykes, A., Wong, F.K., Peters, J., et al. (2015). Human-specific gene ARHGAP11B promotes basal progenitor amplification and neocortex expansion. Science *347*, 1465–1470.

Fricano, C.J., Despensa, T., Jr., Frazel, P.W., Li, M., O'Malley, A.J., Westbrook, G.L., and Luikart, B.W. (2014). Fatty acids increase neuronal hypertrophy of Pten knockdown neurons. Front. Mol. Neurosci. *7*, 30.

Garcez, P.P., Loiola, E.C., Madeiro da Costa, R., Higa, L.M., Trindade, P., Delvecchio, R., Nascimento, J.M., Brindeiro, R., Tanuri, A., and Rehen, S.K. (2016). Zika virus impairs growth in human neurospheres and brain organoids. Science *352*, 816–818.

Geschwind, D.H., and Rakic, P. (2013). Cortical evolution: judge the brain by its cover. Neuron *80*, 633–647.

Groszer, M., Erickson, R., Scripture-Adams, D.D., Lesche, R., Trumpp, A., Zack, J.A., Kornblum, H.I., Liu, X., and Wu, H. (2001). Negative regulation of neural stem/progenitor cell proliferation by the Pten tumor suppressor gene in vivo. Science *294*, 2186–2189.

Hansen, D.V., Lui, J.H., Parker, P.R., and Kriegstein, A.R. (2010). Neurogenic radial glia in the outer subventricular zone of human neocortex. Nature *464*, 554–561.

Hazin, A.N., Poretti, A., Turchi Martelli, C.M., Huisman, T.A., Di Cavalcanti Souza Cruz, D., Tenorio, M., van der Linden, A., Pena, L.J., Brito, C., Gil, L.H., et al.; Microcephaly Epidemic Research Group (2016). Computed Tomographic Findings in Microcephaly Associated with Zika Virus. N. Engl. J. Med. *374*, 2193–2195.

Hill, R., and Wu, H. (2009). PTEN, stem cells, and cancer stem cells. J. Biol. Chem. *284*, 11755–11759.

Juanes, M., Guercio, G., Marino, R., Berensztein, E., Warman, D.M., Ciaccio, M., Gil, S., Bailez, M., Rivarola, M.A., and Belgorosky, A. (2015). Three novel IGF1R mutations in microcephalic patients with prenatal and postnatal growth impairment. Clin. Endocrinol. (Oxf.) *82*, 704–711.

Kornack, D.R., and Rakic, P. (1998). Changes in cell-cycle kinetics during the development and evolution of primate neocortex. Proc. Natl. Acad. Sci. USA *95*, 1242–1246.

Kriegstein, A., Noctor, S., and Martínez-Cerdeño, V. (2006). Patterns of neural stem and progenitor cell division may underlie evolutionary cortical expansion. Nat. Rev. Neurosci. *7*, 883–890.

Kuida, K., Zheng, T.S., Na, S., Kuan, C., Yang, D., Karasuyama, H., Rakic, P., and Flavell, R.A. (1996). Decreased apoptosis in the brain and premature lethality in CPP32-deficient mice. Nature *384*, 368–372.

Kuida, K., Haydar, T.F., Kuan, C.Y., Gu, Y., Taya, C., Karasuyama, H., Su, M.S., Rakic, P., and Flavell, R.A. (1998). Reduced apoptosis and cytochrome c-mediated caspase activation in mice lacking caspase 9. Cell *94*, 325–337.

Kwon, C.H., Luikart, B.W., Powell, C.M., Zhou, J., Matheny, S.A., Zhang, W., Li, Y., Baker, S.J., and Parada, L.F. (2006). Pten regulates neuronal arborization and social interaction in mice. Neuron *50*, 377–388.

Lambeth, C.R., White, L.J., Johnston, R.E., and de Silva, A.M. (2005). Flow cytometry-based assay for titrating dengue virus. J. Clin. Microbiol. *43*, 3267–3272.

Lancaster, M.A., Renner, M., Martin, C.A., Wenzel, D., Bicknell, L.S., Hurles, M.E., Homfray, T., Penninger, J.M., Jackson, A.P., and Knoblich, J.A. (2013). Cerebral organoids model human brain development and microcephaly. Nature *501*, 373–379.

Lee, J.H., Huynh, M., Silhavy, J.L., Kim, S., Dixon-Salazar, T., Heiberg, A., Scott, E., Bafna, V., Hill, K.J., Collazo, A., et al. (2012). De novo somatic mutations in components of the PI3K-AKT3-mTOR pathway cause hemimegalencephaly. Nat. Genet. *44*, 941–945.

Lehtinen, M.K., Zappaterra, M.W., Chen, X., Yang, Y.J., Hill, A.D., Lun, M., Maynard, T., Gonzalez, D., Kim, S., Ye, P., et al. (2011). The cerebrospinal fluid provides a proliferative niche for neural progenitor cells. Neuron *69*, 893–905.

Lengner, C.J., Gimelbrant, A.A., Erwin, J.A., Cheng, A.W., Guenther, M.G., Welstead, G.G., Alagappan, R., Frampton, G.M., Xu, P., Muffat, J., et al. (2010). Derivation of pre-X inactivation human embryonic stem cells under physiological oxygen concentrations. Cell *141*, 872–883.

Li, Y., Wang, H., Muffat, J., Cheng, A.W., Orlando, D.A., Lovén, J., Kwok, S.M., Feldman, D.A., Bateup, H.S., Gao, Q., et al. (2013). Global transcriptional and translational repression in human-embryonic-stem-cell-derived Rett syndrome neurons. Cell Stem Cell *13*, 446–458.

Lui, J.H., Hansen, D.V., and Kriegstein, A.R. (2011). Development and evolution of the human neocortex. Cell *146*, 18–36.

Lui, J.H., Nowakowski, T.J., Pollen, A.A., Javaherian, A., Kriegstein, A.R., and Oldham, M.C. (2014). Radial glia require PDGFD-PDGFRβ signalling in human but not mouse neocortex. Nature *515*, 264–268.

Marchese, M., Conti, V., Valvo, G., Moro, F., Muratori, F., Tancredi, R., Santorelli, F.M., Guerrini, R., and Sicca, F. (2014). Autism-epilepsy phenotype with macrocephaly suggests PTEN, but not GLIALCAM, genetic screening. BMC Med. Genet. *15*, 26.

Mirzaa, G.M., Rivière, J.B., and Dobyns, W.B. (2013). Megalencephaly syndromes and activating mutations in the PI3K-AKT pathway: MPPH and MCAP. Am. J. Med. Genet. C. Semin. Med. Genet. *163C*, 122–130.

Onorati, M., Li, Z., Liu, F., Sousa, A.M., Nakagawa, N., Li, M., Dell'Anno, M.T., Gulden, F.O., Pochareddy, S., Tebbenkamp, A.T., et al. (2016). Zika Virus Disrupts Phospho-TBK1 Localization and Mitosis in Human Neuroepithelial Stem Cells and Radial Glia. Cell Rep. *16*, 2576–2592.

Poduri, A., Evrony, G.D., Cai, X., Elhosary, P.C., Beroukhim, R., Lehtinen, M.K., Hills, L.B., Heinzen, E.L., Hill, A., Hill, R.S., et al. (2012). Somatic activation of AKT3 causes hemispheric developmental brain malformations. Neuron *74*, 41–48.

Qian, X., Nguyen, H.N., Song, M.M., Hadiono, C., Ogden, S.C., Hammack, C., Yao, B., Hamersky, G.R., Jacob, F., Zhong, C., et al. (2016). Brain-Region-Specific Organoids Using Mini-bioreactors for Modeling ZIKV Exposure. Cell *165*, 1238–1254.

Rakic, P. (1974). Neurons in rhesus monkey visual cortex: systematic relation between time of origin and eventual disposition. Science *183*, 425–427.

Rakic, P. (1988). Specification of cerebral cortical areas. Science *241*, 170–176.

Rash, B.G., Tomasi, S., Lim, H.D., Suh, C.Y., and Vaccarino, F.M. (2013). Cortical gyrification induced by fibroblast growth factor 2 in the mouse brain. J. Neurosci. *33*, 10802–10814.

Rivière, J.B., Mirzaa, G.M., O'Roak, B.J., Beddaoui, M., Alcantara, D., Conway, R.L., St-Onge, J., Schwartzentruber, J.A., Gripp, K.W., Nikkel, S.M., et al.; Finding of Rare Disease Genes (FORGE) Canada Consortium (2012). De novo germline and postzygotic mutations in AKT3, PIK3R2 and PIK3CA cause a spectrum of related megalencephaly syndromes. Nat. Genet. *44*, 934–940.

Sasai, Y. (2013). Next-generation regenerative medicine: organogenesis from stem cells in 3D culture. Cell Stem Cell *12*, 520–530.

Stahl, R., Walcher, T., De Juan Romero, C., Pilz, G.A., Cappello, S., Irmler, M., Sanz-Aquela, J.M., Beckers, J., Blum, R., Borrell, V., and Götz, M. (2013). Trnp1 regulates expansion and folding of the mammalian cerebral cortex by control of radial glial fate. Cell *153*, 535–549.

Stelzer, Y., Shivalila, C.S., Soldner, F., Markoulaki, S., and Jaenisch, R. (2015). Tracing dynamic changes of DNA methylation at a single-cell resolution. Cell *163*, 218–219.

Sun, T., and Hevner, R.F. (2014). Growth and folding of the mammalian cerebral cortex: from molecules to malformations. Nat. Rev. Neurosci. *15*, 217–232.

Takahashi, K., Okita, K., Nakagawa, M., and Yamanaka, S. (2007). Induction of pluripotent stem cells from fibroblast cultures. Nat. Protoc. *2*, 3081–3089.

Tang, H., Hammack, C., Ogden, S.C., Wen, Z., Qian, X., Li, Y., Yao, B., Shin, J., Zhang, F., Lee, E.M., et al. (2016). Zika Virus Infects Human Cortical Neural Progenitors and Attenuates Their Growth. Cell Stem Cell *18*, 587–590.

Terrone, G., Voisin, N., Abdullah Alfaiz, A., Cappuccio, G., Vitiello, G., Guex, N., D'Amico, A., James Barkovich, A., Brunetti-Pierri, N., Del Giudice, E., and Reymond, A. (2016). De novo PIK3R2 variant causes polymicrogyria, corpus callosum hyperplasia and focal cortical dysplasia. Eur. J. Hum. Genet. *24*, 1359–1362.

Tokuda, S., Mahaffey, C.L., Monks, B., Faulkner, C.R., Birnbaum, M.J., Danzer, S.C., and Frankel, W.N. (2011). A novel Akt3 mutation associated with enhanced kinase activity and seizure susceptibility in mice. Hum. Mol. Genet. *20*, 988–999.

Worby, C.A., and Dixon, J.E. (2014). Pten. Annu. Rev. Biochem. *83*, 641–669.

Yu, J., Vodyanik, M.A., Smuga-Otto, K., Antosiewicz-Bourget, J., Frane, J.L., Tian, S., Nie, J., Jonsdottir, G.A., Ruotti, V., Stewart, R., et al. (2007). Induced pluripotent stem cell lines derived from human somatic cells. Science *318*, 1917–1920.

STAR★METHODS

KEY RESOURCES TABLE

REAGENT or RESOURCE	SOURCE	IDENTIFIER
Antibodies		
See Table S1	This study	N/A
Chemicals, Peptides, and Recombinant Proteins		
Dorsomorphin	Stemgent	04-0024
GDC-0068	Selleckchem	S2808
MK-2206	Selleckchem	S1078
Critical Commercial Assays		
CellTiter-Glo Luminescent Cell Viability Assay	Promega	G7571
CellEvent Caspase-3/7 Green Detection Reagent	Invitrogen	C10423
Click-iT EdU Imaging Kit	Invitrogen	C10337
TSA Plus Cyanine 3 System	Perkin Elmer	NEL744001KT
Experimental Models: Cell Lines		
Human: WIBR1/2/3 hESCs	Lengner et al., 2010	N/A
Human: WIBR1/2/3 PTEN mutant hESCs	This study	N/A
Mouse: V6.5 mESCs	Stelzer et al., 2015	N/A
Mouse: V6.5 Pten mutant mESCs	This study	N/A
Sequence-Based Reagents		
Primers: see Table S2	This study	N/A

CONTACT FOR REAGENT AND RESOURCE SHARING

Further information and requests for reagents may be directed to, and will be fulfilled by the Lead Contact, Dr. Rudolf Jaenisch (jaenisch@wi.mit.edu).

EXPERIMENTAL MODEL AND SUBJECT DETAILS

ESC culture

HESC lines WIBR1, WIBR2 and WIBR3 were previously described (Lengner et al., 2010; Li et al., 2013) and cultured in 5% O2 on mitomycin C-inactivated mouse embryonic fibroblasts (MEFs) in hESC medium, containing DMEM/F12 (Invitrogen), 15% fetal bovine serum (Hyclone), 5% knockout serum replacement (Invitrogen), 1% non-essential amino acids (Invitrogen), 1mM glutamine (Invitrogen), 0.1mM b-mercaptoethanol (Sigma) and 4ng/ml bFGF (R&D Systems). Cultures were passaged manually or with 1mg/ml collagenase type IV (Invitrogen) every 5-7 days. Mouse ESC line V6.5 was expanded on MEFs using mESC medium containing fetal bovine serum and leukemia inhibitory factor as previously reported (Stelzer et al., 2015).

All experiments involving cells from human subjects were performed in compliance with MIT COHUES protocol 0612002068.

METHOD DETAILS

Neural differentiation

Differentiation of hESCs to NPs in 2D adherent culture was performed as previously described (Li et al., 2013). Confluent hESCs were passaged onto matrigel-coated dishes using collagenase type IV, and cultured in mTeSR medium (Stem Cell Technologies) containing dorsomorphin (2.5uM, Stemgent) for 1-3 days until near confluent. To induce neural differentiation, increasing amounts of N2 media (25, 50, 75, 100%) were added to the mTeSR medium every other day while maintaining 2.5uM dorsomorphin. N2 medium contains 1X N2 supplement (Invitrogen), 50% DMEM/F12, 50% Neurobasal, 0.075% Bovine serum albumin, and 2mM GlutaMAX (Life Technologies). Cells were subsequently passaged with trypsin and cultured on matrigel-coated dishes in N2 media with the addition of 20ng/ml bFGF. Rho-associated protein kinase (ROCK) inhibitor Y27632 (10uM, Stemgent) was added to the medium for the first 24 hr. NPs were expanded and maintained in N2 medium with 20ng/ml bFGF. All 2D culture experiments were performed on WIBR3-derived NPs unless otherwise specified.

CRISPR/Cas9 gRNA design

To generate gRNA expression vector, annealed oligonucleotides for the human or mouse PTEN exon 1 locus were ligated into the BbsI restriction site of a modified pX330 vector containing a CMV-EGFP cassette. The gRNA sequence for human PTEN was 5′-aaa caaaaggagatatcaag-3′, which contains an EcoRV restriction site. The gRNA sequence for mouse Pten was 5′-agatcgttagcagaaa caaaagg-3′. To evaluate the targeting efficiency of human PTEN gene, the CRISPR/Cas9 construct was transiently transfected into HEK293 cells, and PCR fragment was generated from genomic DNA followed by EcoRV restriction digest to evaluate targeting efficiency, using primers described in Table S2. Cel-1 assay was used to evaluate the efficiency of gRNA toward the mouse Pten gene as previously described (Li et al., 2013).

CRISPR/Cas9-mediated genome editing of ESCs

CRISPR/Cas9-mediated genome editing in hESCs was performed as previously described with modifications (Li et al., 2013). Briefly, WIBR3 hESCs were cultured in ROCK inhibitor Y27632 (10uM) for 24 hr prior to electroporation. Cells were harvested using trypsin/EDTA solution and re-suspension in phosphate buffered saline (PBS) as single cells. Electroporation was performed using 25ug of gRNA expression vector and 25ug of PGK-puro plasmid. Cells were plated on DR4 MEFs, and cultured in hESC medium containing ROCK inhibitor Y27632 for the first 24 hr. Puromycin (2ug/ml) was added to hESC medium 48 hr after electroporation for 2 days, and culture was maintained in hESC medium until colonies emerged. Individual hESC clones were picked and expanded 14 days after electroporation. PCR on genomic DNA and EcoRV restriction digest were performed to identify candidate clones, followed by DNA sequencing. CRISPR/Cas9-mediated genome editing in mESCs was performed as previously described (Stelzer et al., 2015).

Cerebral organoid culture

Cerebral organoids were generated from WIBR3 hESCs using a previously reported protocol (Lancaster et al., 2013), with some modifications. Briefly, hESCs were dissociated from MEFs using collagenase type IV, and further separated from residual MEFs by gravity separation, before trypsinization of hESC colonies to generate single cells. A total of 9000 cells were then plated into each well of an ultra-low-attachment 96-well plate (Corning) to form single EBs, in medium containing DMEM/F12, 20% KSR, 3% fetal bovine serum, 2mM GlutaMAX, 1% non-essential amino acids, 50nM b-mercaptoethanol and 4ng/ml bFGF. ROCK inhibitor Y27632 (50uM) was included in the first 24 hr. EBs were maintained in 96-well plates for 6 days, then transferred to ultra-low-attachment 24-well plates (Corning), in neural induction medium containing DMEM/F12, 1X N2 supplement, 1% non-essential amino acids, 2mM GlutaMAX and 1ug/ml heparin (Stem Cell Technologies). On days 10-12, EBs were embedded in droplets of matrigel, and were allowed to gel at 37C. Embedded EBs were subsequently cultured in neural maturation medium containing 50% DMEM/F12, 50% Neurobasal, 0.5X N2 supplement, 0.5X B27 supplement, 2mM GlutaMAX, 2.5ng/ml human insulin, 0.5% non-essential amino acids, and 25nM b-mercaptoethanol. Droplets were cultured in stationary condition in 6cm suspension dishes for 4 days, followed by transfer to an orbital shaker (Unimax-1010, Heidolph Brinkmann) rotating continuously at 80rpm. Mouse cerebral organoids were generated as previously described (Lancaster et al., 2013). Multiple independent experiments were performed to generate cerebral organoids from WIBR1 ($n = 3$), WIBR2 ($n = 3$), WIBR3 ($n > 15$) and V6.5 ($n = 3$). Each experiment generates 24-96 individual organoids of each condition (genotype and treatment). Various concentrations of AKT inhibitors GDC-0068 (Selleckchem) or MK-2206 (Selleckchem) were added to growth medium for EBs on day 1. To pre-pattern organoids toward the dorsal forebrain fate, 2.5uM dorsomorphin was added to the culture on day 0 for 7 or 14 days. To stimulate phospho-AKT in 12-week organoids, BDNF (100ng/ml, Peprotech) was added for 30 min. All human cerebral organoid experiments were performed on WIBR3-derived control and mutant lines unless otherwise specified.

Lentivirus production and transduction

FUW-GFP, FUW-GFP-PTEN lentivirus constructs were previously reported (Fricano et al., 2014). DN-AKT and CA-AKT cDNA were subcloned into FUW-GFP vector to generate the FUW-DN-AKT and FUW-CA-AKT lentivirus constructs. VSVG-coated lentiviruses were generated in HEK293 cells. Briefly, HEK293 cells were transfected using X-tremeGENE 9 (Sigma), with a mixture of lentiviral construct and second-generation packaging plasmids. Culture medium was changed 12 hr after and collected 96 hr after transfection. Virus-containing medium was filtered through 0.45um filter and concentrated via ultracentrifugation. To transduce hESCs with lentivirus, hESCs cultured on MEFs were first dissociated from MEFs using collagenase type IV, and further dissociated using Trypsin/EDTA to generate single cells. hESCs were plated onto matrigel-coated dishes and fed mTeSR medium containing 10uM ROCK inhibitor Y27632, and lentivirus particles. hESCs were subsequently passaged as single cells at clonal density to MEFs, and single clones were manually picked and expanded. Expression of lentiviral-transgenes was evaluated using GFP fluorescent, quantitative RT-PCR and immuno-blotting.

ZIKV and Dengue virus production and infection

ZIKV strain MR766 was obtained from ATCC and expanded in Vero cells. Dengue virus serotype 2 strain 16681 was expanded in C3/36 mosquito cells. To establish titered viral stocks, virus-containing cell supernatants were harvested, and viral titer was determined by infecting Vero cells, followed by quantitative flow cytometry analysis of Flavivirus envelope immuno-staining (Lambeth et al., 2005) to calculate Vero cell infectious units. To infect cerebral organoids, the number of cells on the surface was estimated from the diameter of the 3D organoid and was used to calculate the amount of virus applied. An MOI of 1 based on Vero cell infectious units was used for all experiments for ZIKV and Dengue virus (actual MOI for the entire organoid was greatly less than 0.01). ZIKV or Dengue virus was added to culture medium and replaced with fresh medium 24 hr later. Organoids were analyzed 4 or 10 days post-infection.

ATP assay

Cell growth rate was measured using an ATP assay with the CellTiter-Glo Luminescent kit according to the manufacturer's instructions (Promega). NPs were plated in matrigel-coated 96-well plates (black wall, clear bottom, Falcon) at 20,000 cells per well, in the presence or absence of bFGF (0-20ng/ml), PDGF-DD (0-10ng/ml) or IGF2 (0-10ng/ml). ATP assay was performed on day 1 and day 3. Luminescence was recorded on a Tecan microplate reader.

EdU click-it assay

EdU (10uM, Life Technologies) was added to N2 medium for NPs, or neural maturation medium for cerebral organoids for 2 hr, after which cells or tissues were collected immediately, or washed with PBS and fed fresh medium until collection. N2 medium contained 1 or 20ng/ml of bFGF. EdU click-it assay was performed on fixed cells or tissue sections per manufacture's instruction (Invitrogen), followed by immuno-staining.

Histology and imaging

Cells and tissues were fixed with 4% (w/v) paraformaldehyde in PBS. Frozen or paraffin sections were prepared from tissues (EBs and organoids). Following membrane permeabilization with PBS containing 0.3% triton, cells and tissue sections were blocked with 3% normal donkey serum. Primary antibodies were against Brn2, Cleaved-caspase 3, Ctip2, Doublecortin, Flavivirus, FoxA2, FoxG1, GFAP, phospho-H3, HOPX, Ki67, Nkx2.2, NeuN, Nestin, PAX6, phospho-AKT, Satb2, Sox2, Tau, Tbr1, Tbr2, TH, phospho-Vimentin, and visualized by secondary antibodies conjugated with Alexa 488, 568, 594, 647 (Life Technologies), followed by counter-staining with DAPI. Detailed antibody information is described in Table S1. Tyramide Signal Amplification was performed using TSA Plus Cyanine 3 System per manufacturer's instruction (Perkin Elmer). Detection of activated caspase 3/7 in live organoids was performed using a CellEvent Caspase-3/7 Green Detection Reagent (ThermoFisher). Fluorescent images of immuno-staining were captured on a Zeiss LSM-700 confocal microscope. Light-sheet fluorescent microscopy was performed on Hoechst-stained organoids using a Zeiss Z.1 Lightsheet microscope. Reconstruction of multi-view light sheet images was performed using ZEN (Zeiss) and Imaris (Bitplane) softwares. Quantification of volume, surface area and sphericity were performed using Imaris. Alternatively, stereological quantification was performed on every 5 section of organoids, stained with DAPI. The area of the organoid and the length of the outline were measured to calculate volume and surface area. A Canny Edge Detection plugin of ImageJ was used to measure fold density in images of Hoechst-stained organoids, some were manually stitched from multiple images.

RNA extraction, reverse transcription and quantitative PCR

Cells and tissues were homogenized and total RNA extracted using the RNeasy kit (QIAGEN) following manufacturer's instructions. Total RNA concentrations were measured using NanoDrop ND-1000 spectrophotometer. RNA was reverse transcribed into cDNA using Superscript III reverse transcriptase (Invitrogen) with random hexamer primers according. Transcript abundance was determined by quantitative PCR using SYBR Green PCR mix (Applied Biosystems), with primer pairs against ARHGAP11B, BRN2, CTIP2, CUX1, CUX2, DCX, FOXA2, HOPX, MAP2, MKI67, NKX2.2, PAX6, RBFOX3, SATB2, TBR1, TBR2, TUBB3 and GAPDH. Primer sequences are described in Table S2. Raw Ct values were normalized to GAPDH. Heatmap visualization of quantitative PCR results was generated using gene-E software.

Protein purification and immuno-blotting

Total protein was extracted from cells and tissues using RIPA lysis buffer (Millipore) containing 50mM Tris-HCL pH 7.4, 150mM NaCL, 0.25% deoxycholic acid 1% NP-40, 1mM EDTA, protease inhibitor cocktail (Roche), phosphotase inhibitor cocktail 2 and 3 (Sigma). Total protein from the supernatant was measured using BCA protein assay (Pierce). Primary antibodies were against Actin, PTEN, phospho-AKT, AKT, and visualized with HRP-conjugated secondary antibodies, followed by LumiGlo Chemiluminescent Kit (KPL) in accordance with the manufacturer's instructions. Detailed antibody information is described in Table S1. Membranes blotted for phospho-proteins were stripped and re-probed with antibodies against total proteins. Quantification of band intensity was performed using ImageJ. Values for phospho-proteins were normalized to total proteins, and all others were normalized to Actin.

Analysis of BrainSpan data

Gene expression data was obtained from the BrainSpan Prenatal LMD Microarray database, which contains transcriptional profiling of ~300 distinct brain regions from human prenatal brain. Expression levels of genes of interest at week 15-16 were aggregated according to top-level structure designation, and plotted based on z-scores.

QUANTIFICATION AND STATISTICAL ANALYSIS

All data values were presented as mean ± SEM. Student's t tests were applied to data with two groups. ANOVA analyses were used for comparisons of data with greater than two groups. Post hoc group comparisons were performed with Bonferroni test. A value of $p < 0.05$ was considered significant.

Cell Stem Cell, Volume *20*

Supplemental Information

Induction of Expansion and Folding in Human Cerebral Organoids

Yun Li, Julien Muffat, Attya Omer, Irene Bosch, Madeline A. Lancaster, Mriganka Sur, Lee Gehrke, Juergen A. Knoblich, and Rudolf Jaenisch

Supplemental Information

Inventory of Supplemental Information

Figure S1

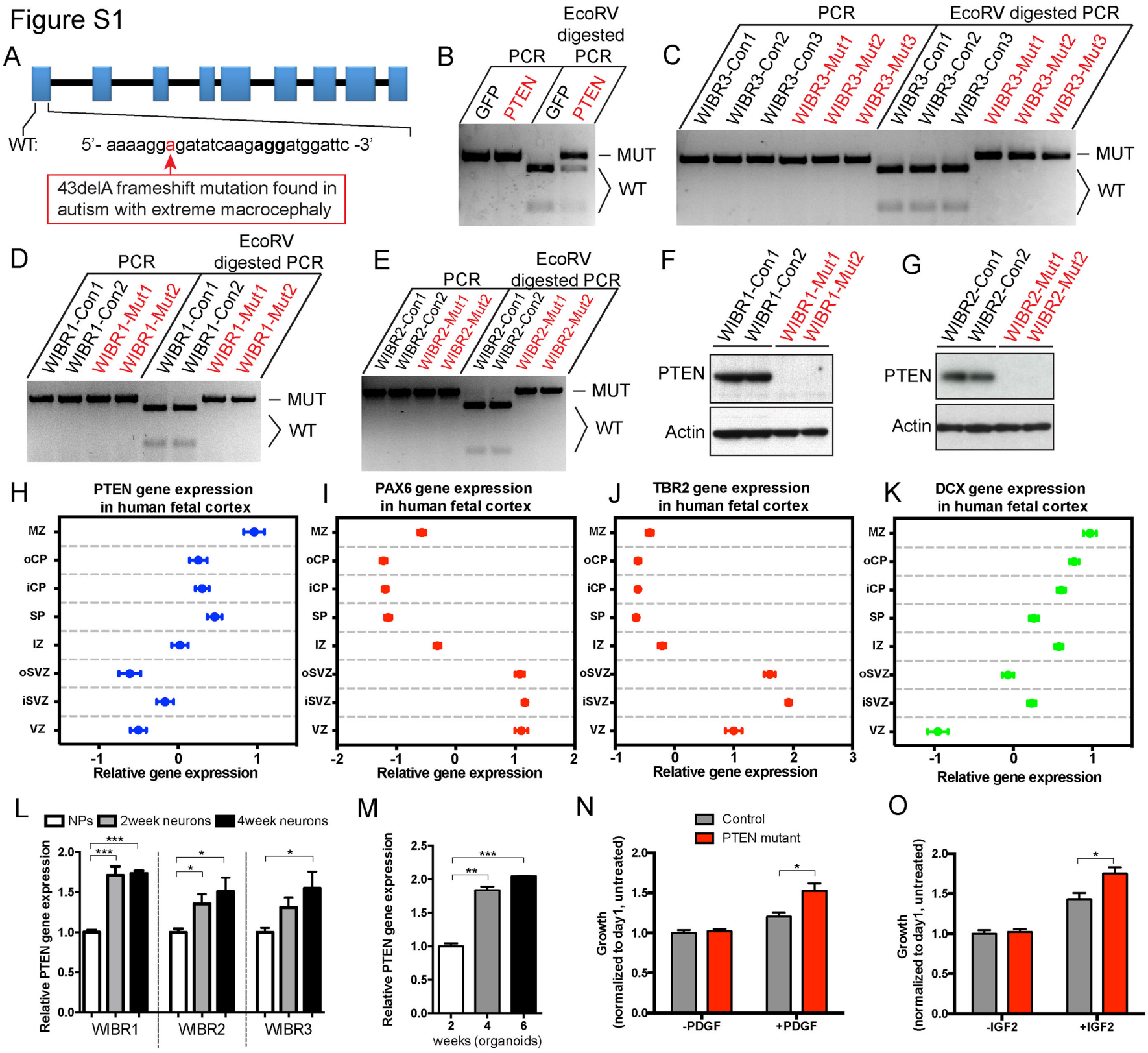
A
WT: 5'- aaaaggagatatcaaggaggatggattc -3'
43delA frameshift mutation found in autism with extreme macrocephaly
B
PCR
EcoRV digested PCR
GFP
PTEN
GFP
PTEN
MUT
WT
C
PCR
EcoRV digested PCR
WIBR3-Con1
WIBR3-Con2
WIBR3-Con3
WIBR3-Mut1
WIBR3-Mut2
WIBR3-Mut3
MUT
WT
D
PCR
EcoRV digested PCR
WIBR1-Con1
WIBR1-Con2
WIBR1-Mut1
WIBR1-Mut2
MUT
WT
E
PCR
EcoRV digested PCR
WIBR2-Con1
WIBR2-Con2
WIBR2-Mut1
WIBR2-Mut2
MUT
WT
F
WIBR1-Con1
WIBR1-Con2
WIBR1-Mut1
WIBR1-Mut2
PTEN
Actin
G
WIBR2-Con1
WIBR2-Con2
WIBR2-Mut1
WIBR2-Mut2
PTEN
Actin
H
PTEN gene expression in human fetal cortex
MZ
oCP
iCP
SP
IZ
oSVZ
iSVZ
VZ
Relative gene expression
I
PAX6 gene expression in human fetal cortex
Relative gene expression
J
TBR2 gene expression in human fetal cortex
Relative gene expression
K
DCX gene expression in human fetal cortex
Relative gene expression
L
NPs
2week neurons
4week neurons
Relative PTEN gene expression
WIBR1
WIBR2
WIBR3
M
Relative PTEN gene expression
weeks (organoids)
N
Control
PTEN mutant
Growth (normalized to day1, untreated)
-PDGF
+PDGF
O
Growth (normalized to day1, untreated)
-IGF2
+IGF2

Figure S1. CRISPR/Cas9-mediated deletion of *PTEN* in hESCs, and *PTEN* expression analysis. Related to Figure 1.

A) Schematic overview of the human *PTEN* locus showing the heterozygous 43delA loss-of-function mutation identified in autism patient with macrocephaly(Marchese et al., 2014).

B) Gel images showing EcoRV digest results from HEK293 cells transfected with PTEN CRISPR/Cas9 and mock control with GFP plasmid. Indels generated in the target regions may lead to disruption of the EcoRV site.

C-E) Gel images showing disruption of the EcoRV site in *PTEN* mutant clones generated from WIBR3 (C), WIBR1 (D) and WIBR2 (E) hESCs.

F-G) Immuno-blotting showing a complete ablation of wild-type PTEN protein in *PTEN* mutant clones from WIBR1 (F) and WIBR2 (G) hESCs.

H-K) Analysis of BrainSpan gene expression data of *PTEN* (H), *PAX6* (I), *TBR2* (J) and *DCX* (K) shows *PTEN* expression is low in the VZ/SVZ of the human cortex at 15 or 16 post conception weeks, and high in the cortical plate (CP), a spatial pattern similar to *DCX* and inversely correlated with *PAX6* and *TBR2*. IZ, intermediate zone; SP, subplate zone, MZ, marginal zone.

L-M) Quantitative RT-PCR analyses of *PTEN* in NPs, 2-week and 4-week neurons generated from WIBR1, WIBR2 and WIBR3 hESCs (L), and in WIBR3 cerebral organoids at 2, 4 and 6 weeks of age (M).

N-O) ATP assay on 2D adherent NP culture, showing enhanced proliferation in WIBR3 *PTEN* mutants in the presence of low PDGF (N) and IGF2 (O) concentration.

Results are mean +/- SEM. *$p<0.05$, ***$p<0.001$.

Figure S2

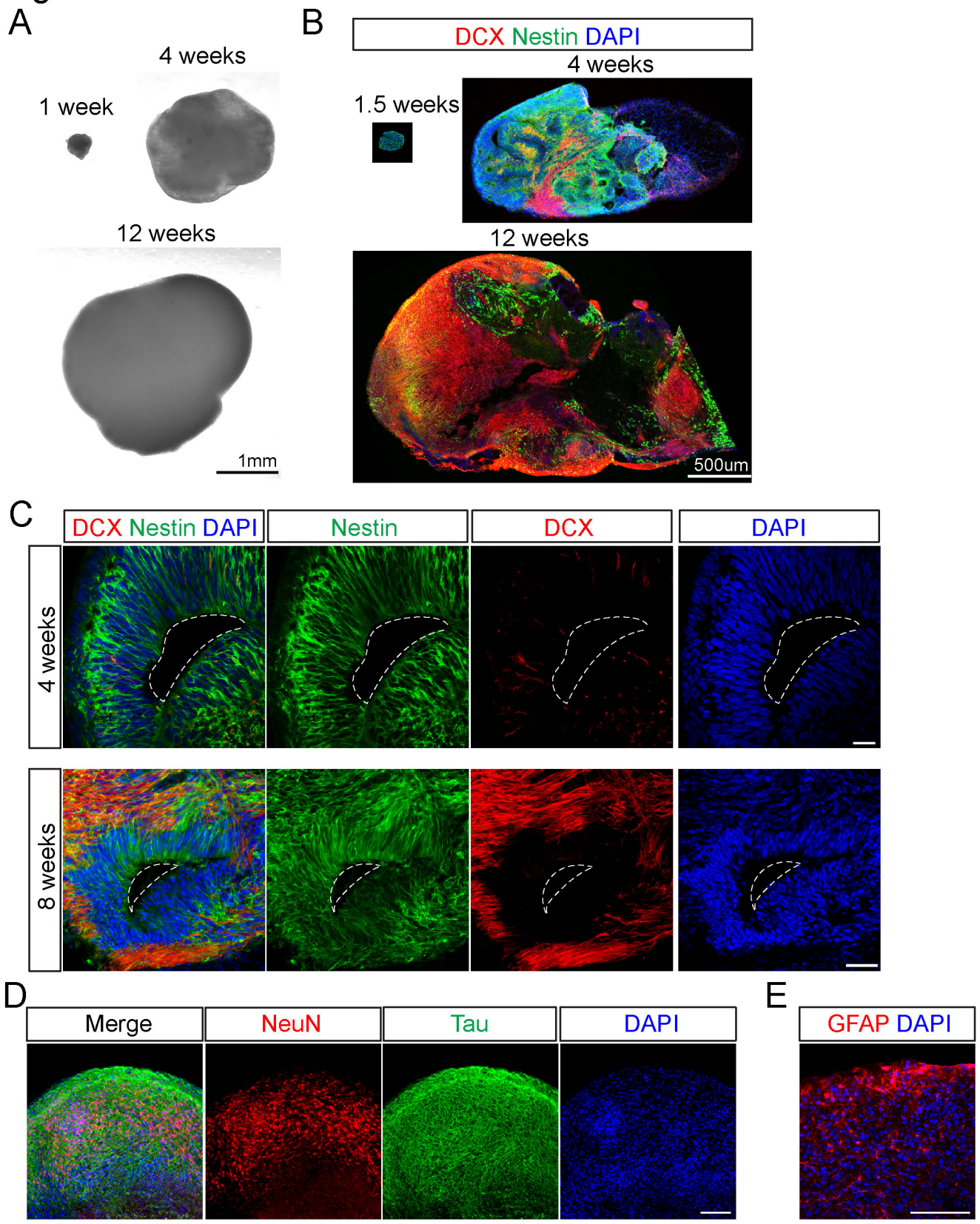
A
4 weeks
1 week
12 weeks
1mm
B
DCX Nestin DAPI
4 weeks
1.5 weeks
12 weeks
500um
C
DCX Nestin DAPI
Nestin
DCX
DAPI
4 weeks
8 weeks
D
Merge
NeuN
Tau
DAPI
E
GFAP DAPI

Figure S2. Generation of human cerebral organoid culture. Related to Figure 1.

A) Representative images of human cerebral organoids from wild-type WIBR3 hESCs at 1, 4 and 12 weeks. Scale bar, 1mm.

B-C) Immuno-staining with antibodies against DCX (immature neurons, red) and Nestin (NPs, green), on human cerebral organoids from wild-type WIBR3 hESCs at 1.5, 4 and 12 weeks. Low magnification images (B) demonstrate the global transition from NPs to neurons. High magnification images (C) show representative ventricle-like structures at 4 and 8 weeks, highlighting the appearance of DCX-positive immature neurons at the latter stage, and the basal location of these cells. Scale bars, 500um (B) and 50um (C).

D-E) Immuno-staining in 16-weeks-old cerebral organoids generated from wild-type WIBR3 hESCs showing abundant expression of markers for mature neurons such as NeuN and Tau (D) and astrocytes (GFAP, E). Scale bars, 100um.

Figure S3

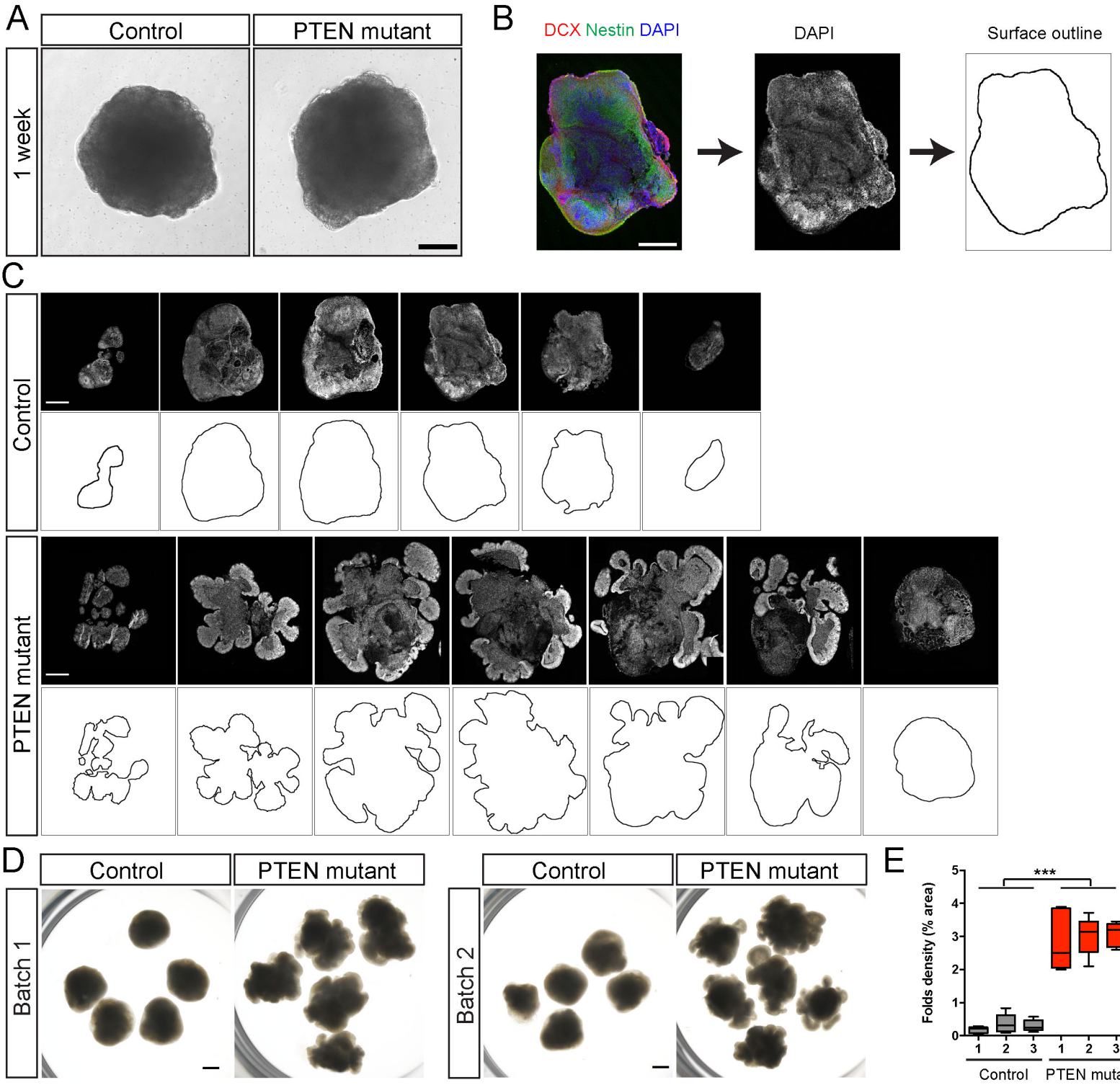
A
Control
PTEN mutant
1 week
B
DCX Nestin DAPI
DAPI
Surface outline
C
Control
PTEN mutant
D
Control
PTEN mutant
Control
PTEN mutant
Batch 1
Batch 2
E
***
Folds density (% area)
0
1
2
3
4
5
1
2
3
1
2
3
Control
PTEN mutant

Figure S3. Morphological analysis of expansion and folding in *PTEN* mutant human cerebral organoids. Related to Figure 1.

A) Representative images of EBs generated from control and *PTEN* mutant WIBR3 hESCs at 1 week, showing their similar size and shape at this stage. Scale bar, 200um.

B-C) Images of serial histological sections from 6-week-old control and *PTEN* mutant WIBR3 cerebral organoids were converted into outlines for the quantification of total volume, and surface area. Scale bars, 100um.

D) Images of multiple WIBR3 organoids generated from two independent experiments showing morphological differences between control and *PTEN* mutants at 6 weeks of age. Scale bars, 1mm.

E) Quantification of surface folds density in Hoechst-stained control and *PTEN* mutant WIBR3 cerebral organoids from 3 independent experiments.

Results are mean +/- SEM. ***$p<0.001$.

Figure S4

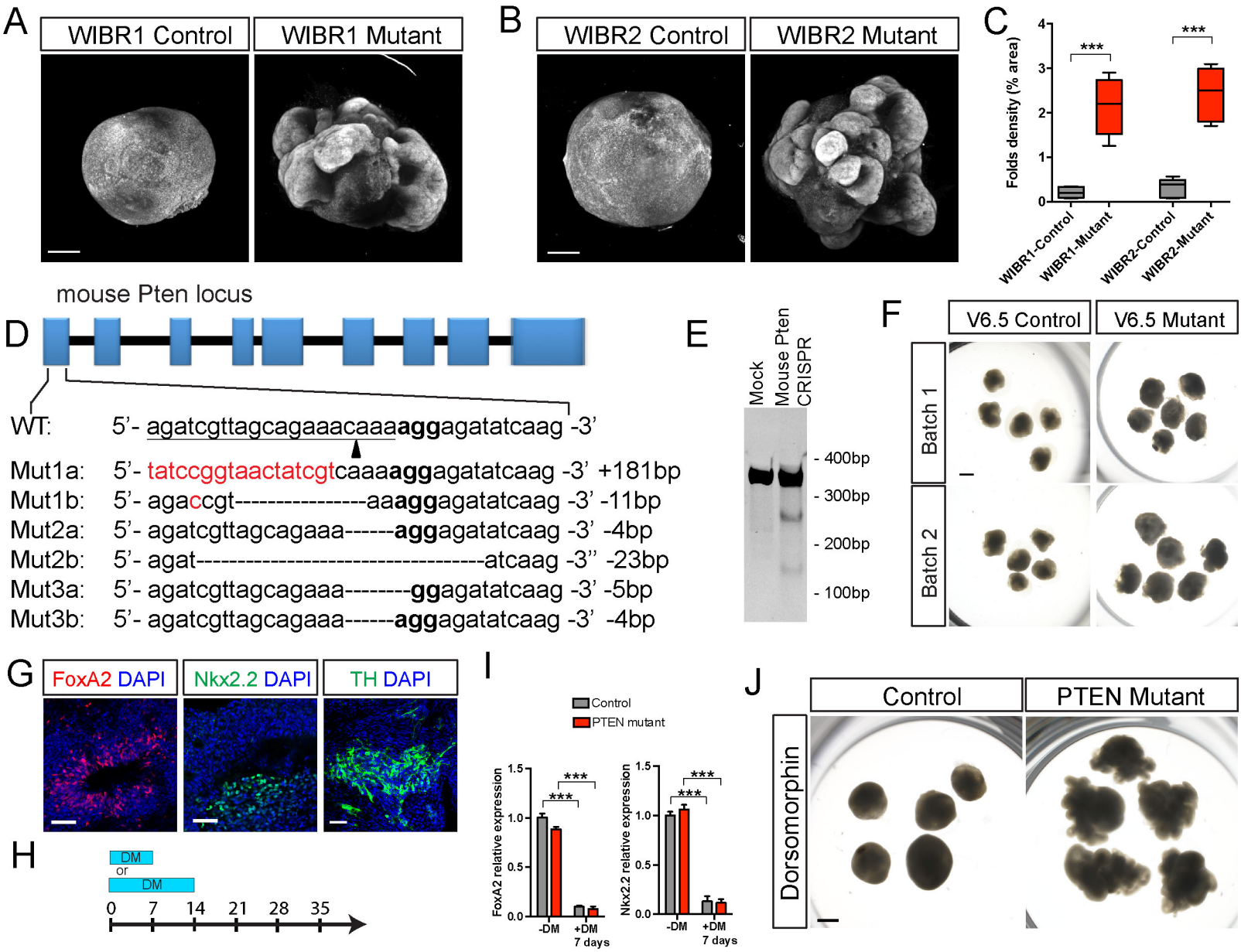
A
WIBR1 Control
WIBR1 Mutant
B
WIBR2 Control
WIBR2 Mutant
C
Folds density (% area)
***
***
WIBR1-Control
WIBR1-Mutant
WIBR2-Control
WIBR2-Mutant
mouse Pten locus
D
WT: 5'- agatcgttagcagaaacaaaaggagatatcaag -3'
Mut1a: 5'- tatccggtaactatcgtcaaaaggagatatcaag -3' +181bp
Mut1b: 5'- agaccgt----------aaaggagatatcaag -3' -11bp
Mut2a: 5'- agatcgttagcagaaa------aggagatatcaag -3' -4bp
Mut2b: 5'- agat----------atcaag -3'' -23bp
Mut3a: 5'- agatcgttagcagaaa--------ggagatatcaag -3' -5bp
Mut3b: 5'- agatcgttagcagaaa------aggagatatcaag -3' -4bp
E
Mock
Mouse Pten CRISPR
- 400bp
- 300bp
- 200bp
- 100bp
F
V6.5 Control
V6.5 Mutant
Batch 1
Batch 2
G
FoxA2 DAPI
Nkx2.2 DAPI
TH DAPI
H
DM
or
DM
0 7 14 21 28 35
I
Control
PTEN mutant
FoxA2 relative expression
Nkx2.2 relative expression
***
***
-DM
+DM
7 days
J
Control
PTEN Mutant
Dorsomorphin

Figure S4. *PTEN* mutant human and mouse cerebral organoids. Related to Figure 1, 2 and 3.

A-B) Light sheet images of Hoechst-stained control and *PTEN* mutant human cerebral organoids generated from WIBR1 (A) and WIBR2 (B) hESCs. Scale bar, 500um.

C) Quantification of surface folds density in Hoechst-stained control and *PTEN* mutant human cerebral organoids from WIBR1 and WIBR2.

D) Schematic overview of the mouse *Pten* locus and sequences of mutant V6.5 mouse ESC clones,

E) Gel picture of Cel-1 assay with gRNA against mouse *Pten* gene.

F) Images of multiple mouse control and *Pten* mutant organoids at 6 weeks of age, generated from two independent experiments. Scale bars, 1mm.

G) Immuno-staining with antibodies against FoxA2, Nkx2.2 and TH on human cerebral organoids from wild-type WIBR3 hESCs.

H) Schematic diagram of dorsomorphin (DM) treatment during the first 7 or 14 days of organoid culture.

I) Quantitative RT-PCR for FoxA2 and Nkx2.2 shows dorsomorphin (DM) treatment for 7 days suppressed the expression of these none forebrain markers.

J) Images of multiple control and *PTEN* mutant WIBR3 cerebral organoids treated with dorsomorphin for the first 14 days. Scale bars, 1mm.

Results are mean +/- SEM. ***p<0.001.

Figure S5

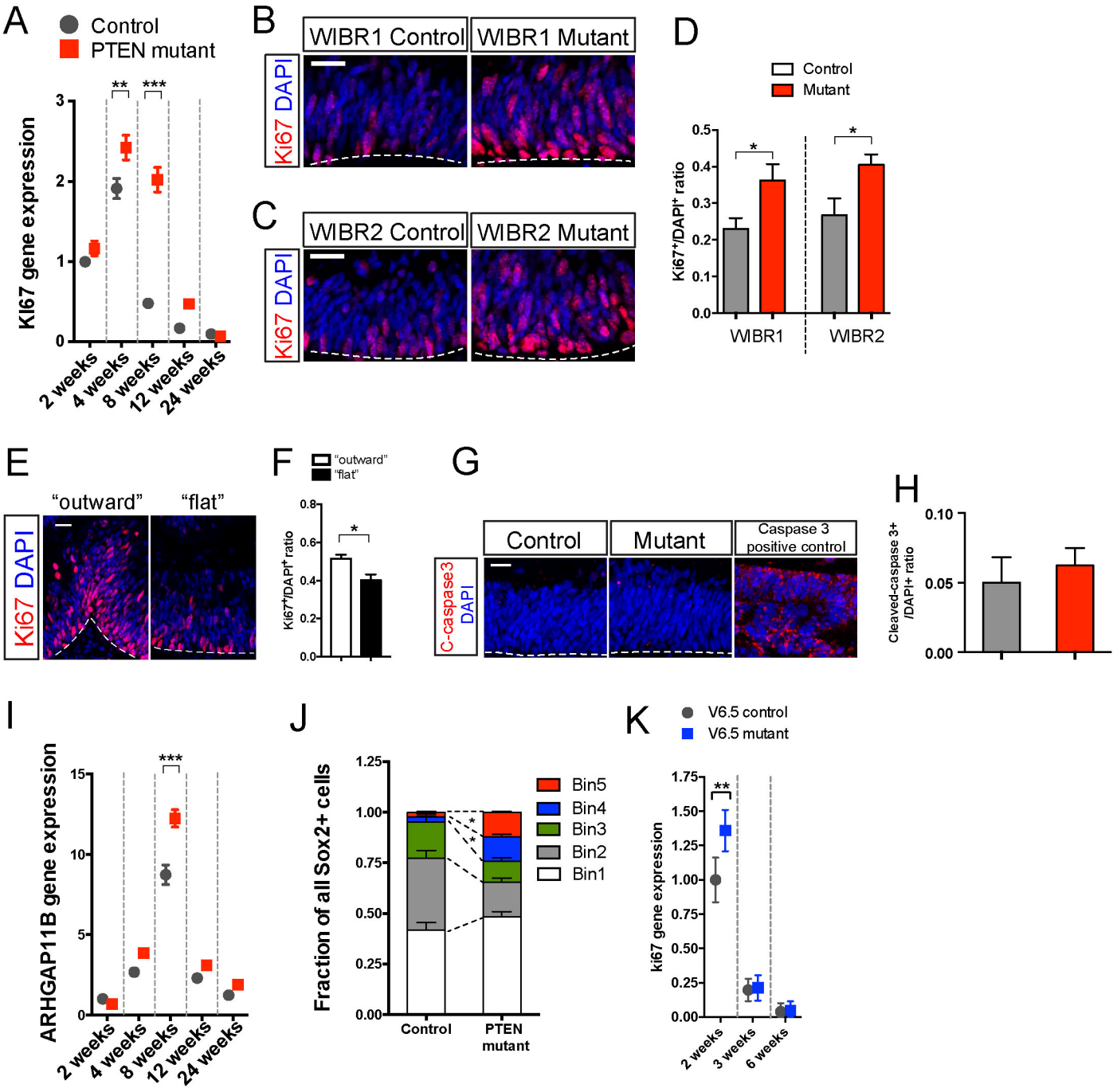
A
Control
PTEN mutant
Ki67 gene expression
2 weeks
4 weeks
8 weeks
12 weeks
24 weeks
B
WIBR1 Control
WIBR1 Mutant
Ki67 DAPI
C
WIBR2 Control
WIBR2 Mutant
D
Control
Mutant
Ki67+/DAPI+ ratio
WIBR1
WIBR2
E
"outward"
"flat"
F
G
Control
Mutant
Caspase 3 positive control
C-caspase3 DAPI
H
Cleaved-caspase 3+ /DAPI+ ratio
I
ARHGAP11B gene expression
J
Fraction of all Sox2+ cells
Bin5
Bin4
Bin3
Bin2
Bin1
Control
PTEN mutant
K
V6.5 control
V6.5 mutant
ki67 gene expression
2 weeks
3 weeks
6 weeks

Figure S5. Enhancing proliferation in *PTEN* mutant human cerebral organoids expands the NP pool. Related to Figure 4.

A) Quantitative RT-PCR analysis of proliferation marker *KI67* demonstrates their temporal-specific over-expression in *PTEN* mutant WIBR3 cerebral organoids compared to controls.

B-D) Representative images and quantification of Ki67 immuno-staining in control and *PTEN* mutant WIBR3 cerebral organoids generated from WIBR1 and WIBR2. Scale bar, 20um.

E-F) Representative images (E) and quantification (F) of Ki67 immuno-staining in *PTEN* mutant WIBR3 cerebral organoids with outward curvature or flat. Scale bar, 20um.

G-H) Representative images (G) and quantification (H) of cleaved-caspase 3 (c-caspase 3) immuno-staining in control and *PTEN* mutant WIBR3 cerebral organoids. Positive control is a day 34 organoid after 4 days of ZIKV exposure (see later, Figure 7). Scale bar, 20um.

I) Quantitative RT-PCR analyses of *ARHGAP11B* in control and *PTEN* mutant WIBR3 cerebral organoids.

J) Distribution of Sox2+ NPs in the neuroepithelium of *PTEN* mutant WIBR3 cerebral organoids is significantly enriched towards the basal surface, compared to controls.

K) Quantitative RT-PCR for *Ki67* in mouse organoids shows mutants had increased expression at 2 weeks but not 3 or 6 weeks.

Results are mean +/- SEM. *p<0.05, **p<0.01, ***p<0.001.

Figure S6

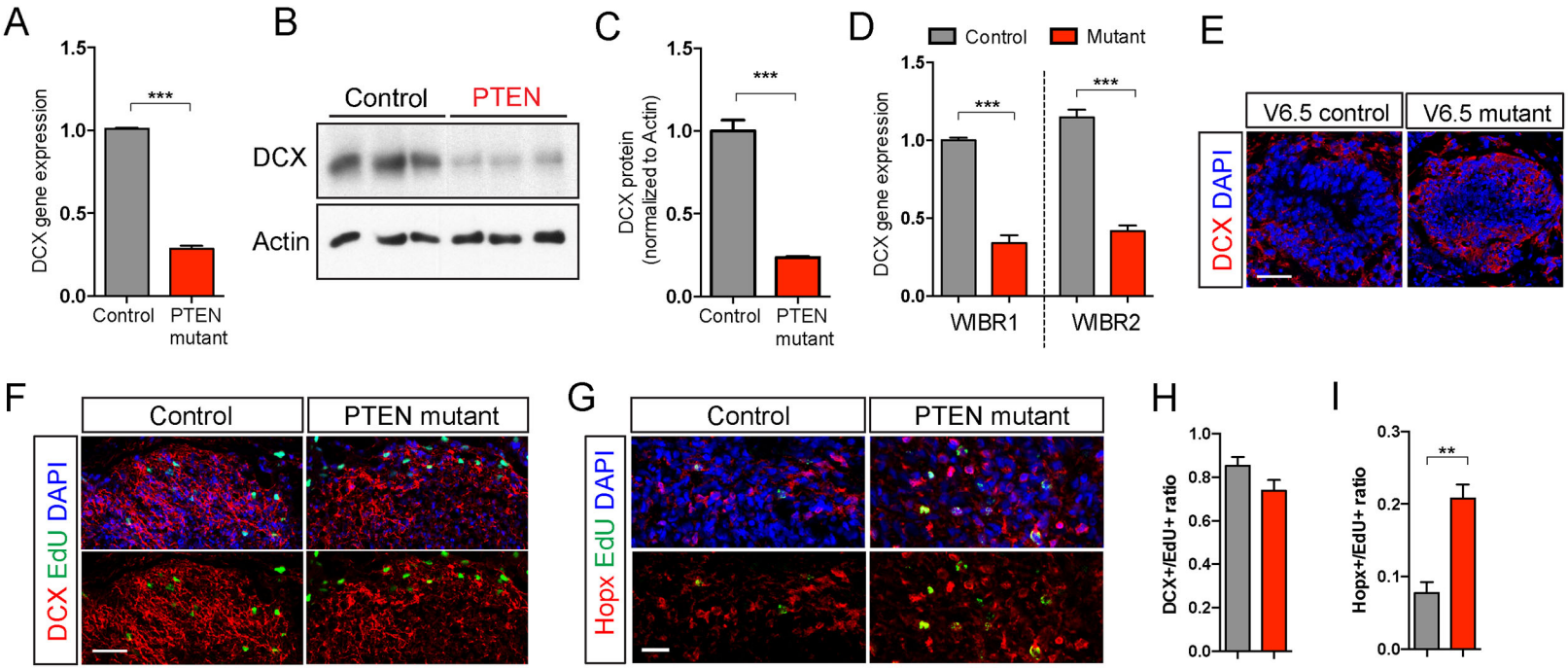
A
DCX gene expression
1.5
1.0
0.5
0.0
***
Control
PTEN mutant
B
Control
PTEN
DCX
Actin
C
DCX protein (normalized to Actin)
1.5
1.0
0.5
0.0
***
Control
PTEN mutant
D
Control
Mutant
DCX gene expression
1.5
1.0
0.5
0.0
***
***
WIBR1
WIBR2
E
V6.5 control
V6.5 mutant
DCX DAPI
F
Control
PTEN mutant
DCX EdU DAPI
G
Control
PTEN mutant
Hopx EdU DAPI
H
DCX+/EdU+ ratio
1.0
0.8
0.6
0.4
0.2
0.0
I
Hopx+/EdU+ ratio
0.3
0.2
0.1
0.0
**

Figure S6. Transiently delayed neuronal differentiation in *PTEN* mutant human cerebral organoids. Related to Figure 5.

A-C) *PTEN* mutant cerebral organoids at 4 weeks showed delayed neuronal differentiation, as measured by reduced *DCX* mRNA (A) and protein (B-C) levels.

D) Delayed neuronal differentiation in 4-week-old *PTEN* mutant cerebral organoids from WIBR1 and WIBR2 as measured by *DCX* gene expression.

E) Immuno-staining for DCX in 3-week-old control and *Pten* mutant mouse organoids shows comparable levels of expression.

F-I) Representative images and quantification of immuno-staining for EdU (labeled at 4 weeks) and DCX (F) or Hopx (G) in 8-week old organoids. Majority of EdU+ cells co-localized with DCX (H), albeit a significantly more co-labeled with Hopx in the *PTEN* mutant WIBR3 cerebral organoids compared to control (I). Scale bars, 50um (F) and 20um (G).

Results are mean +/- SEM. **p<0.01, ***p<0.001.

Figure S7

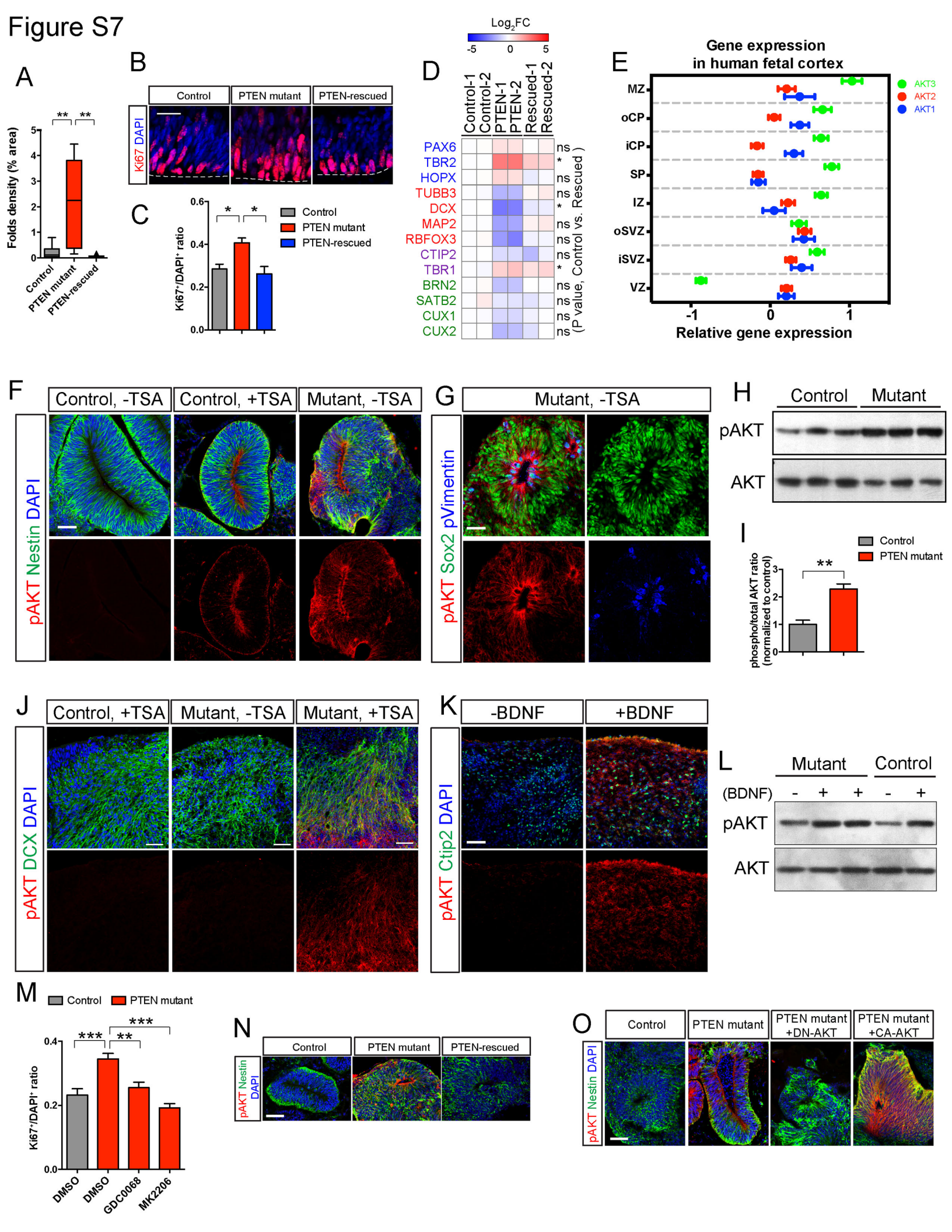
A
Folds density (% area)
Control
PTEN mutant
PTEN-rescued
B
Control
PTEN mutant
PTEN-rescued
Ki67 DAPI
C
Ki67+/DAPI+ ratio
Control
PTEN mutant
PTEN-rescued
D
Log2FC
Control-1
Control-2
PTEN-1
PTEN-2
Rescued-1
Rescued-2
PAX6
TBR2
HOPX
TUBB3
DCX
MAP2
RBFOX3
CTIP2
TBR1
BRN2
SATB2
CUX1
CUX2
(P value, Control vs. Rescued)
E
Gene expression in human fetal cortex
MZ
oCP
iCP
SP
IZ
oSVZ
iSVZ
VZ
AKT3
AKT2
AKT1
Relative gene expression
F
Control, -TSA
Control, +TSA
Mutant, -TSA
pAKT Nestin DAPI
G
Mutant, -TSA
pAKT Sox2 pVimentin
H
Control
Mutant
pAKT
AKT
I
Control
PTEN mutant
phospho/total AKT ratio (normalized to control)
J
Control, +TSA
Mutant, -TSA
Mutant, +TSA
pAKT DCX DAPI
K
-BDNF
+BDNF
pAKT Ctip2 DAPI
L
Mutant
Control
(BDNF)
pAKT
AKT
M
Control
PTEN mutant
Ki67+/DAPI+ ratio
DMSO
DMSO
GDC0068
MK2206
N
Control
PTEN mutant
PTEN-rescued
pAKT Nestin DAPI
O
Control
PTEN mutant
PTEN mutant +DN-AKT
PTEN mutant +CA-AKT
pAKT Nestin DAPI

Figure S7. PTEN-AKT signaling in human cerebral organoids. Related to Figure 6.

A) Quantitative analysis of the density of surface folds in control, *PTEN* mutant, and PTEN-rescued WIBR3 cerebral organoids at 6 weeks.

B-C) Representative images and quantification of Ki67 immuno-staining in control, *PTEN* mutant, and PTEN-rescued WIBR3 cerebral organoids at 6 weeks. Scale bar, 20um.

D) Differential gene expression analyses by quantitative RT-PCR on control, *PTEN* mutant, and PTEN-rescued WIBR3 cerebral organoids at 6 weeks. Gene expressions are normalized to control-1. P value reflects controls vs. PTEN-rescued mutants.

E) Analysis of BrainSpan gene expression data shows *AKT1*, *AKT2* and *AKT3* are expressed in the human cortex at 15 or 16 pcw.

F) Immuno-staining with tyramide signal amplification (TSA) allowed detection of pAKT in control WIBR3 cerebral organoids, showing enrichment towards the apical surface of the VZ, a similar pattern as seen in *PTEN* mutants without TSA. Scale bar, 50um.

G) Immuno-staining in *PTEN* mutant WIBR3 cerebral organoids shows co-localization of pAKT and NP markers Sox2 and phospho-Vimentin (pVimentin). Scale bar, 50um.

H-I) Immuno-blotting analysis shows increased pAKT protein level in *PTEN* mutant WIBR3 cerebral organoids at 6 weeks.

J) Immuno-staining with TSA allowed detection of pAKT in DCX+ neurons of 8-week-old *PTEN* mutant WIBR3 cerebral organoids, no significant signal was detected in controls with or without TSA. Scale bars 50um.

K) Immuno-staining for pAKT and Ctip2 shows acute treatment with BDNF (30') increased pAKT immuno-staining in 12-week-old *PTEN* mutant WIBR3 cerebral organoids, without TSA. Scale bar, 50um.

L) Immuno-blotting analysis shows increased pAKT protein level upon BDNF treatment in 12-week-old control and mutant organoids.

M) Quantification of Ki67 immuno-staining shows AKT inhibitors GDC-0068 (1uM) or MK-2206 (100nM) reduced proliferation in *PTEN* mutant WIBR3 cerebral organoids.

N-O) Cerebral organoids generated from *PTEN* mutants transduced with *GFP-PTEN* lentivirus (N) or *DN-AKT* (O) showed reduced pAKT immuno-staining compared to

PTEN mutants alone, whereas *CA-AKT* transduced mutants showed high level of pAKT. Scale bars, 50um.

Results are mean +/- SEM. *p<0.05, **p<0.01, ***p<0.001.

Table S1. Antibody information. Related to Figure 1-7.

S1a. Antibodies for immuno-staining

Antibody	Vendor	Catalog #	Species	Dilution
Phospho-AKT	Cell Signaling	4058	Rabbit	1:100
Brn2	Santa Cruz	sc6029	Goat	1:500
Cleaved-caspase 3	Cell Signaling	9661	Rabbit	1:1000
Ctip2	Abcam	ab18465	Rat	1:500
Doublecortin	Santa Cruz	sc-8066	Goat	1:500
Flavivirus	Santa Cruz	sc-71122	Mouse	1:100
FoxA2	R&D Systems	AF2400	Goat	1:300
FoxG1	Abcam	ab18259	Rabbit	1:500
GFAP	Dako	z0334	Rabbit	1:1000
Phospho-Histone H3	Millipore	06-570	Rabbit	1:1000
HOPX	Santa Cruz	sc-30216	Rabbit	1:500
Ki67	Dako	M7240	Mouse	1:100
Nkx2.2	Santa Cruz	sc-15015	Goat	1:500
Nestin	Millipore	MAB5326	Mouse	1:300
NeuN	Millipore	MAB377	Mouse	1:300
Pax6	Covance	PRB-278P	Rabbit	1:300
Satb2	Abcam	ab51502	Mouse	1:300
Sox2	R&D Systems	AF2018	Goat	1:300
Tau	Dako	A0024	Rabbit	1:500
Tbr1	Abcam	ab31940	Rabbit	1:500
Tbr2	Abcam	ab23345	Rabbit	1:300
Tbr2	Millipore	AB15894	Chicken	1:300
TH	Pel-freez	P40101	Rabbit	1:500
Phospho-Vimentin	MBL	D076-3	Mouse	1:1000

S1b. Antibodies for immuno-blotting

Antibody	Vendor	Catalog #	Species	Dilution
Actin	Sigma	A2228	Mouse	1:1000
Phospho-AKT	Cell Signaling	4058	Rabbit	1:1000
AKT	Cell Signaling	9272	Rabbit	1:1000
PTEN	Cell Signaling	9559	Rabbit	1:1000

Table S2. Primer information. Related to Figure 3-6.

S2a. Primers for quantitative PCR

Gene	Primer (forward)	Primer (reverse)
Arhgap11b	AGAAAAGAAGGGCGTGTACC	TTCTTCAAAGCCTTCCAGTGA
Brn2	CGGCGGATCAAACTGGGATTT	TTGCGCTGCGATCTTGTCTAT
Ctip2	GAGTACTGCGGCAAGGTGTT	TAGTTGCACAGCTCGCACTT
Cux1	GCTCTCATCGGCCAATCACT	TCTATGGCCTGCTCCACGT
Cux2	AAGGAGATCGAGTCGCAGAA	CTCCAGGATGCTCTTGATGG
Dcx	TCCCGGATGAATGGGTTGC	GCGTACACAATCCCCTTGAAGTA
FoxA2	TGGGAGCGGTGAAGATGGAAGGGCAC	TCATGCCAGCGCCCACGTACGACGAC
Gapdh	CGTGGAAGGACTCATGACCA	CAGTCTTCTGGGTGGCAGTGA
Hopx	GAGACCCAGGGTAGTGATTTGA	AAAAGTAATCGAAAGCCAAGCAC
Map2	CTCAGCACCGCTAACAGAGG	CATTGGCGCTTCGGACAAG
Mki67 (human)	ACGCCTGGTTACTATCAAAAGG	CAGACCCATTTACTTGTGTTGGA
Mki67 (mouse)	ATCATTGACCGCTCCTTTAGGT	GCTCGCCTTGATGGTTCCT
Nkx2.2	TGCCTCTCCTTCTGAACCTTGG	GCGAAATCTGCCACCAGTTG
Pax6	ACCCATTATCCAGATGTGTTTGCCCGAG	ATGGTGAAGCTGGGCATAGGCGGCAG
Pten	TGGATTCGACTTAGACTTGACCT	TGGCGGTGTCATAATGTCTTTC
Rbfox3	CCAAGCGGCTACACGTCTC	CGTCCCATTCAGCTTCTCCC
Satb2	CCTCCTCCGACTGAAGACAG	TGGTCTGGGTACAGGCCTAC
Tbr1	ATGGGCAGATGGTGGTTTTA	GACGGCGATGAACTGAGTCT
Tbr2	CACCGCCACCAAACTGAGAT	CGAACACATTGTAGTGGGCAG
Tubb3	GGCCAAGGGTCACTACACG	GCAGTCGCAGTTTTCACACTC

S2b. Primers for genotyping PCR

Gene	Primer (forward)	Primer (reverse)
Pten (human genomic)	AGCAGCTTCTGCCATCTCTC	TAGCCCTCAGGAAGAGACCA
Pten (mouse genomic)	GAGCCATTTCCATCCTGCAG	CTAGCCGAACACTCCCTAGG